Static and Fatigue Analysis of Wind Turbine Blades Subject to Cold Weather Conditions Using Finite Element Analysis

by

Patricio Andres Lillo Gallardo
B.Sc., Catholic University of Chile, 1999
M.Sc., Catholic University of Chile, 2001

A Thesis Submitted in Partial Fulfillment of the
Requirements for the Degree of

MASTER OF APPLIED SCIENCES

in the Department of Mechanical Engineering

Static and Fatigue Analysis of Wind Turbine Blades Subject to Cold Weather Conditions Using Finite Element Analysis

by

Patricio Andres Lillo Gallardo
B.Sc., Catholic University of Chile, 1999
M.Sc., Catholic University of Chile, 2001

Supervisory Committee

Dr. Curran Crawford, Supervisor
(Department of Mechanical Engineering)

Dr. Bradley Buckham, Departmental Member
(Department of Mechanical Engineering)

Dr. Chris Papadopoulos , Outside Member
(Department of Electrical Engineering)

Supervisory Committee

Dr. Curran Crawford, Supervisor
(Department of Mechanical Engineering)

Dr. Bradley Buckham, Departmental Member
(Department of Mechanical Engineering)

Dr. Chris Papadopoulos , Outside Member
(Department of Electrical Engineering)

ABSTRACT

Canada has aggressive targets for introducing wind energy across the country, but also faces challenges in achieving these goals due to the harsh Canadian climate. One issue which has received little attention in other countries not experiencing these extremes is the behaviour of composite blades in winter conditions. The scope of the work presented is to analyze the static stresses and fatigue response in cold climates using finite element models of the blade.

The work opens with a quantification of the extremes of cold experienced in candidate Canadian wind turbine deployment locations. The thesis then narrows its focus to a consideration of the stresses in the root of the composite blades, specifically two common blade-hub connection methods: embedded root carrots and T-bolts. Finite element models of the root are proposed to properly simulate boundary conditions, applied loading and thermal stresses for a 1.5 MW wind turbine. It is shown that the blade root is strongly affected by the thermal stresses caused by the mismatch and orthotrophy of the coefficients of thermal expansion of the blade root constituents.

Fatigue analysis of a blade is then presented using temperature dependent material properties including estimated fatigue coefficients.It was found that the natural frequencies of a 1.5 MW wind turbine blade are not significantly altered at cold temperatures. Additionally, cold temperatures slightly increase stresses in the composite blade skin when the blade is loaded, due to an increase in stiffness. Cold temperatures also lead to higher cyclic flapwise bending moments acting on the blade. However,

this increase was found not to affect the lifetime fatigue damage. Finally, it was found that the cold climate as seen in Canada improves the fatigue strength of the saturated composite materials used in the blade. The predicted fatigue damage of the triaxial fabric and the spar cap layers in cold climates was therefore predicted to be half that of the fatigue damage at room temperature. This is caused solely by the temperature dependence of the fatigue coefficient b which requires further experimental verification to validate the numerical results of the current study.

Contents

List of Tables

List of Figures

Nomenclature

1-direction	Fibre-direction (unidirectional composite)
2-direction	In-plane and perpendicular to fibre direction (unidirectional composite)
3-direction	Out-of-plane and perpendicular to fibre direction (unidirectional composite)
E_1	Young's modulus 1-direction
E_2	Young's modulus 2-direction
E_3	Young's modulus 3-direction
ν_{12}	Poisson's ratio
G_{12}	Shear modulus
σ_1	1-direction normal stress
σ_2	2-direction normal stress
σ_3	3-direction normal stress
σ_{12}	Shear stress
σ_{vm}	von Mises stress
σ_1^T	Ultimate tensile strength for 1-direction
σ_2^T	Ultimate tensile strength for 2-direction
σ_3^T	Ultimate tensile strength for 3-direction
σ_1^C	Ultimate compressive strength for 1-direction
σ_2^C	Ultimate compressive strength for 2-direction
σ_3^C	Ultimate compressive strength for 3-direction
σ_Y	Yield strength
τ_{12}^F	Shear strength
V_f	Fibre volume fraction
V_{e1}	1 year return wind speed
V_{e50}	50 year return wind speed
z-direction	0°, aligned with the longitudinal blade axis (off-axis laminates)
x-direction	In-plane and orthogonal with z-direction (off-axis laminates)
y-direction	Out-of-plane and orthogonal with z-direction (off-axis laminates)

List of Acronyms

ASTM	American Society for Testing and Materials
CLD	Constant Life Diagram
CLT	Classical Laminate Theory
CTE	Coefficient of Thermal Expansion
DNV	Det Norske Veritas
ETS	L'Ecole de Technologie Superiéure
FAST	NREL's Aeroelastic Design Code for Horizontal Axis Wind Turbines
FAA	Federal Aviation Administration
FE	Finite Element
FEM	Finite Element Method
FRP	Fiber Reinforced Polymer
HAWT	Horizontal Axis Wind Turbine
HSS	High Speed Shaft
GL	Germanischer Lloyd
GMFD	Global Meteorological Forcing Dataset for Land Surface Modelling
LSS	Low Speed Shaft
IEA	International Energy Agency

IEC	International Electrotechnical Commission
ILSS	Interlaminar Shear Strength
NASA	National Aeronautics and Space Administration
NREL	National Renewable Energy Laboratory
NuMAD	Numerical Manufacturing and Design
NWTC	National Wind Technology Center
SF	Safety Factor
STI	Scientific and Technical Information
UTS	Ultimate Tensile Strength
WESNet	NSERC Wind Energy Strategic Network
WMC	Knowledge Centre Wind Turbine Materials and Constructions

ACKNOWLEDGEMENTS

I wish to thank all those who helped me to complete this project and turned this graduate time into a great experience. Without their support this work may not have been possible. My sincere gratitude to my supervisor Dr. Curran Crawford, for his patience, support, and guidance through all the stages in this learning process. I really appreciate the time Dr. Crawford spent helping me to develop understanding of my subject of study and helping me to solve practical aspects of my work. I would like to extend my thanks to Catalina Lartiga, Shane Cline, Trevor Williams, Mike McWilliam, Eric Hoevenaars, Michael Shives and Arash Akhgari for their advice. My deepest gratitude goes to my family and Catalina, for their love and support over all these years.

I would like to express my appreciation for funding through the NSERC Wind Energy Strategic Network (WESNet) and the National Commission of Scientific and Technological Research of Chile (CONICYT). I wish to acknowledge the contributions of collaborating specialists Laurent Cormier and Simon Joncas at L'Ecole de Technologie Superiéure (ETS) in Montreal.

DEDICATION

To Catalina, a very funny lady.

Chapter 1

Introduction

Currently, wind energy supplies approximately 1% of Canada's electricity production, however the Canadian Wind Association is advocating strategies to increase that amount to 25% by 2025 [1]. Several provinces and electric utility companies have also outlined future plans to significantly increase wind energy generation. For example, in the short term, Manitoba plans to develop 1,000 MW of wind energy from 2009–2014 according to the Manitoba Provincial Government. Quebec Hydro is planning 3,500 MW of wind energy by 2012 [2]. To accomplish these goals, wind turbines will be erected throughout Canada in cold regions that experience extreme conditions in comparison with other cold climate areas already having successful experiences in wind energy, such as Scandinavian countries.

Severe cold weather is known to adversely affect wind turbine performance. Yukon Energy has operated wind turbines since 1993 and has reported a number of critical issues arising from cold conditions, including issues with overhead power lines, pitch bearing and gearbox lubrication, generators, electronic cabinets, anemometers, ice detectors and blade heaters [3]. The Wind Energy in Cold Climates Annex of the International Energy Agency (IEA) has reported critical issues of cold conditions affecting pitch systems, gearboxes, yaw motors, control computer systems and a lack of proven anti-icing and de-icing technology to keep the blades from rime and glaze ice which alter the structural loads on wind turbines [4]. In addition to the component issues noted above, the blade root's behaviour is important to study because of the steel/epoxy/reinforcement interface that will create complicated stress distributions. These critical stresses will arise from heterogeneous coefficients of thermal expansion (CTE), neat resin/grout areas, and the fact that the root experiences the maximum

bending loads in the blade and by design typically has a reduced cross sectional area relative to other blade sections.

In terms of structural analysis, composites with polymeric matrices are a complex group of materials. Figure 1.1 shows an optical microscopy of the E/glass fibers and the epoxy matrix for an unidirectional composite [5]. The unidirectional arrangement of fibers creates an anisotropic state for fibre-direction and perpendicular-to-fibre direction properties.

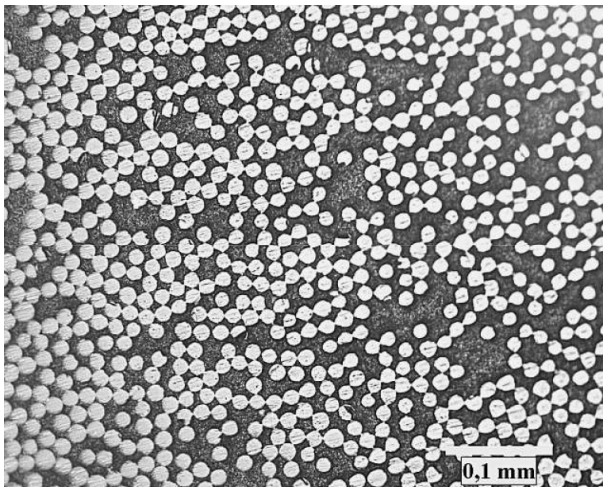

Figure 1.1: Optical microscopy of an unidirectional composite (200X)

External loading can cause multi-axial stresses in off-axis laminates, even when the overall load state is unidirectional. Thermal stresses develop due to the differences in the Coefficients of Thermal Expansion CTE of the composite's fibre and matrix components. It is also important to consider the absorption of water and the subsequent impact of freeze-thaw cycling on composite performance. The factors that affect the detailed behaviour of composites include fibre/matrix interfacial properties, fibre volume fractions, fibre orientations, moduli and Poisson's ratios, load transfer mechanisms, and the fabrication and processing history [6]. In addition, existing research on composite materials focuses on room and cryogenic temperatures (near 50°K). Moreover, there are no universally applicable models capable of predicting composite response under multi-axial loading and environmental effects. Therefore, there is little existing knowledge on composites used for blades when subjected to temperatures and conditions that characterize cold weather [7].

To address these unknowns, the work presented in this thesis focuses on the determination of relevant parameters to define extreme cold conditions in Canada's distinctive regions. This is followed by an estimation of the effects of cold conditions on the static load carrying capabilities of blade root carrots and T-bolt connections using a Finite Element (FE) approach. Finally, the whole-blade dynamic fatigue response at cold temperatures was investigated using a FE model.

1.1 Collaborators Investigation

A parallel experimental investigation program is underway by the authors' collaborators Laurent Cormier and Simon Joncas at L'École de Technologie Superiéure (ETS) in Montreal to expand the database available for material properties in cold conditions [5]. The testing campaign includes both static strength and fatigue performance characterization.

To date, for the case of static strength, the ETS work has determined the strengths of vacuum infused unidirectional E-glass/epoxy composites with V_f of 55%. Tensile, compressive and short beam samples have been tested in eight different environmental conditions, measuring strength, elastic modulus and Poisson's ratios. The test conditions were: fully dried; fully saturated (water); at room temperature and -40°C; either as-is and after 100 thermal cycles between -40°C and 40°C. At least 5 specimens were tested for each condition and all the tests were performed in the fibre direction. Tensile specimens were 3 plies thick, compressive specimens 8 plies thick, and Interlaminar Shear Strength (ILSS) (short beam) specimens were 12 plies thick. The tests were performed according to American Society for Testing and Materials (ASTM) standards.

Composite coupons were also tested under different temperature and moisture conditions for fatigue performance characterization. S-N curves were generated at tensile-tensile loadings of $R = 0.1$ using load control. The composite coupons were also vacuum infused unidirectional E-glass fibre in an epoxy matrix with v_f=57,5%. The eight test conditions were: fully dried; fully saturated (water); at room temperature and -40°C; either as is and after 100 thermal cycles between -40°C and 40°C. The dry samples were fully dried in a vacuum oven. Wet specimens were saturated by immersion in tap water. Saturation occurred near 0.5% by weight.

1.2 Literature Review

Several researchers have studied the effects of cold climate on wind farm operations. Most of the experience comes from Northern and Nordic European countries. The annex Wind Energy in Cold Climates of the IEA has described the issues faced by European wind farms in cold weather, specifically Nordic countries and Switzerland [4]. Another interesting report addressing the Canadian experience was made by Maissan [3], reporting the effects of sub-arctic conditions on wind turbines including rime icing. The work describes the operational history of two wind turbines owned by Yukon Energy near Whitehorse, Yukon. The University of Manitoba is currently developing an extensive body of work on the consequences of rime ice on aerodynamic performance [2], since ice accretion on the blade seems to be a major issue faced in cold climate conditions.

1.2.1 Composite Materials

With respect to composite properties, Mandell and Samborsky [8] provide a substantial source of data for composite performance at room temperatures, both for static and fatigue properties. Several composite combinations and fibre arrangements were tested in that work, as well as incorporating analytical models for engineering properties of composites with different V_f. Those research results for the basis of the composite properties at room temperature used in the current work. Another source of composite data is the OPTIMAT Project from the Knowledge Centre Wind Turbine Materials and Constructions (WMC) [1] .

Unfortunately, relatively little is known about composite performance in cold conditions. Dutta [6] investigated Fiber Reinforced Polymer (FRP) subjected to 50°C and -60°C. Rivera [9] researched the degradation of carbon/vinylester composites for thermally cycled and salt water saturated composites at cold temperatures. Cormier [5] summarized the few predictive models for composites behaviour at low temperature and a provided a detailed list of previous research on fibre reinforced composites at non-cryogenic temperatures. Those analytical models predict that cold temperatures and absorbed moisture reduce strengths through softening, but the complexity of the fibre arrangements makes it difficult to develop a generic model valid for every

[1] www.wmc.eu

case. In additional, the manufacturing processes used and quality control greatly affect composite properties and performance.

Another source of cold temperature testing data is the National Wind Technology Center (NWTC) [10], which tested twelve sub-structure specimens of double-ended wind turbine blade root stud specimens to determine single stud pull-out strengths at arctic temperatures (-50°C). The testing consisted of eleven fatigue tests and one static test. Composite property information is also available from work by Hyer [11] and Kaw [12], which give the coefficient of thermal expansion of several composites at room temperature.

The work presented in this thesis specifically modelled root connections and its constituents made of steel and epoxy. For epoxy properties, Choi [13] and Usami [14] provided data for room and cold temperatures, including cryogenic conditions.

1.2.2 Composite Material Failure Models

There is still controversy around appropriate composite failure theories, since no single methodology fits the data perfectly in all situations. Several models have been developed, specially for application in the aeronautic and astronautic industry. A good detailed summary of composite failure criteria for the modern aerospace industry is presented by the National Aeronautics and Space Administration (NASA) Scientific and Technical Information (STI) program [15] and for the US Federal Aviation Administration (FAA) [16]. Wind turbine design standards also include failure criteria; for example, the Det Norske Veritas (DNV) standards [17] contain a detailed description of criteria to be used for composites. More details on specific criteria used in this work can be found in Azzi and Tsai's work [18, 19] which present the meticulous description of the Tsai-Hill criterion. Christensen [20] and Hashin [21] describe the Hashin criterion for separate matrix and fibre failure formulations.

With respect to fatigue failure, Deggrieck and Van Paepegem [22] classify fatigue models for wind turbine applications into those fatigue life models based on $S-N$ curves and those based on residual strength models. It also presents a review of the major fatigue models and life estimation methodologies. As was mentioned before, Mandell and Samborsky [8] also present fatigue failure models in their work which is extensively presented in [23]. Burton [24] describes common practises in wind turbine design to evaluate fatigue damage. Sutherland [25] studies the agreement of Goodman

diagrams, specifically between linear and bi-linear models, which allows comparison between lifespan prediction methods.

1.2.3 Finite Element (FE) Blade Models

With respect to FE modelling, lately there had been a lot of research on fibre reinforced polymers by means of FE methods. However, applying Finite Element Method (FEM) to wind turbines is still an ongoing area of research. Current development of computer capabilities has increased the feasibility of such research. Even today, to model an entire blade requires a significant amount of computational resources. Szekrenyes [26] summarizes the use of the FEM to study damage and failure of composite materials and structures, focusing on micromechanic modelling of the individual fibres, interfaces and matrix. Kong [27] proposed a structural design including FE work to design a medium scale composite wind turbine blade made of E-glass/epoxy for a 750 kW Horizontal Axis Wind Turbine (HAWT). A prototype E-glass/epoxy blade was tested statically and results were compared with the analytical model using the Tsai-Wu failure criterion, showing good agreement. McKittrick [28] from Sandia National Laboratories designed a 15 meter diameter fibreglass blade through the use of FE modelling. The scope of the work was to minimize resonant operating conditions and to design the blade to withstand extreme wind conditions. The work also included a model to apply a variable pressure on the airfoil section to simulate aerodynamic forces. Paquette [29], also from Sandia National Laboratories, designed a carbon fibre blade using the FEM including several innovative structural features such as flat-back airfoils, a constant thickness carbon spar-cap, and a thin, large diameter root. Also, tests were made to verify the design, undergoing modal, static, and fatigue testing. Other interesting work was elaborated on by Locke [30] who studied hybrid (carbon and e-glass) designs for a 9.2 m prototype wind turbine. The baseline design used unidirectional fibres in combination with $\pm 45°$and random mat layers for the skin and spar cap. The blade was designed using the Numerical Manufacturing and Design (NuMAD) software and solved by means of the FEM evaluated at extreme wind conditions (static).

Samborsky [31] has carried out research into the static and fatigue failure of blade joints using small scale models. FE analysis was used to explore interactions between joint geometry, local stress concentrations and pore locations. Veers [32] described

blade root detail modelling by means of the FEM, including a mesh and joint scheme for a T-bold connection. Other interesting work on small scale FE modelling was made by Deng [33] which applied thermal and mechanical stresses in steel surfaces bonded to FRP materials.

1.3 Thesis Outline and Key Contributions

The remainder of the thesis document presents the work performed on blade analysis. Chapter 2 describes the characteristics of weather conditions in Northern Canada. Regions in Northern Canada were studied taking into account a reasonable possibility of wind turbine installation, and proximity to population centres and/or transmission infrastructure. The nominal turbine configuration used in this study is also presented. The contributions of this chapter are:

- Possible installation regions
- Climate parameters identified for these regions, including minimum daily temperatures and numbers of freeze-thaw cycles

Chapter 3 focuses on the estimation of the effects of cold conditions on the static load carrying capabilities of blade root carrots and T-bolt connections using a FE approach. The contributions are:

- Estimated loads acting on the blade root connections at extreme wind conditions
- Development of a material database for composites properties at cold temperatures
- FE model development and analysis of extreme aerodynamic and thermal loads for static failure

Chapter 4 focuses on whole-blade fatigue response at cold temperatures. A FE model of the entire blade is subjected to fatigue loads distinctive of Northern Canadian weather. The contributions include:

- Estimation of fatigue loads
- Development of a material database for composite properties in fatigue at cold temperatures

- Analysis of vibration natural frequencies, stresses due to increased blade stiffness, root bending moment changes due to increased air density, and lifetime fatigue damage

Although experimental validation of the FE models would have been ideal, or even experimental results for other composite layups in cold conditions, the testing program at L'Ecole de Technologie Superiéure (ETS) is still ongoing and further validation results were unavailable. Although at least one full-scale root carrot test was identified in the literature, the detailed definition of the test specimen was not available due to commercial sensitivities, and therefore it was not possible to validate the models against full-scale tests.

Chapter 5 concludes the presentation by summarizing the results and enumerating avenues for future work.

Chapter 2

Canadian Cold Weather Characterization and Nominal Wind Turbine Definition

2.1 Typical Canadian Conditions

A series of weather parameters were identified as relevant in affecting the static and aerodynamic loads of wind turbine blades, as well as material structural behaviour:

1. Minimum daily winter temperature
2. Number of freeze-thaw cycles per season
3. Temperature gradient associated with daily temperature variation
4. Relative humidity
5. Icing events per year
6. Wind velocity characteristics varying with season

A number of raw data sources for this information were identified, including: the Global Meteorological Forcing Dataset for Land Surface Modelling (GMFD) constructed by the Land Surface Hydrology Research Group of Princeton University [34]; Canada's Wind Energy Atlas developed by the EOLE Wind Energy Project [35]; and the National Climate Data and Information Archive of Canada [36].

The regions studied in this thesis were limited to locales where there is a reasonable possibility of wind turbine installation, constrained by proximity to population centres and/or transmission infrastructure. The GMFD consists of 3-hour interval atmospheric records for the period 1948–2000 containing information on surface temperature, surface wind velocity and surface humidity, among others. The geographic resolution of the database is one degree, which in Canadian latitudes results in an region of 50 km by 50 km.

The distinctive areas were defined by using minimum daily temperature information from the GMFD superimposed on Canada's Wind Energy Atlas grid in ArcGIS software. Figure 2.1 depicts the year mean wind speed in Canada. As can be seen, the North of Canada, the Yukon Territory, the Great Lakes and The Maritime provinces posses outstanding wind speeds.

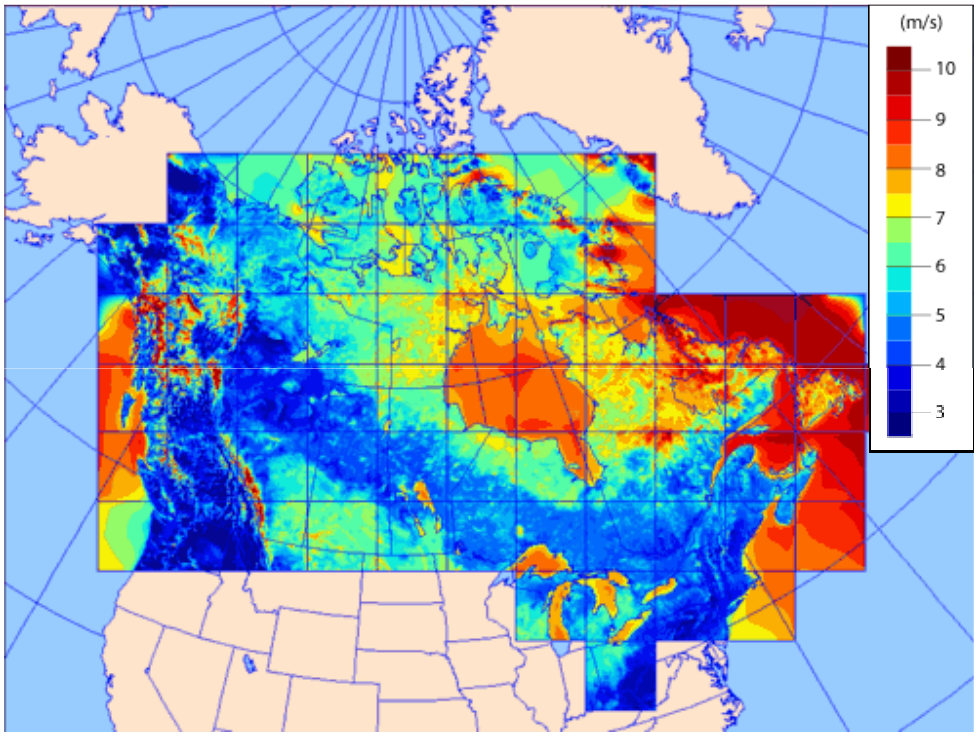

Figure 2.1: Year mean wind speed in Canada at 50 m height. Source; Canada Wind Energy Atlas web site. www.windatlas.ca

GMFD files for the period 1950–2000 were processed using the statistical software R to obtain the weather parameters listed above for the selected locations, including

regions where no ground-base information was available. Among others, some of the selected regions were:

1. Iqaluit, Nunavut (pop. 6,184), is the capital and the biggest city in the province. Nunavut Power Company supplies energy for the province through small diesel generators, consuming 40 million litres of diesel fuel per year, which represents 20% of the total budget of the province. Its dependency on diesel ironically contributes to the climate change that is most affecting these Northern communities.

2. Whitehorse, Yukon Territories (pop. 21,450), is the biggest city in the north of Canada. It has excellent wind conditions and since 1993 Yukon Energy Corporation has produced energy using wind turbines: one 0.15 MW Bonus (installed in 1993) and one 0.66 MW Vestas V47-660 (installed in 2000).

3. Churchill, Manitoba (pop. 1,000) is located on the windy shore of Hudson's Bay; this location is attracting the attention of wind energy companies. In 2006, Westman Wind Power announced its intention to build a wind farm project in the Churchill area. Currently wind tests are being carried out.

4. St. Lawrence Windfarm, Newfoundland, is the easternmost wind farm in Canada (9 3 MW Vestas turbines, total capacity 27 MW). The East coast of Canada is expected to experience a high number of rime ice events. The humidity and atmospheric corrosivity (NaCl) are also higher in comparison to inland sites.

Table 2.1: Summary of extracted weather parameters

	Return		Iqaluit	Whitehorse	Churchill	St. Lawrence
Min. daily winter temp. (°C)	1 yr	Avg.	-29.3	-20.8	-18.9	0.9
		Std. dev.	7.4	8.7	8	3.2
	50 yr	Ext.	-51.1	-49.4	-45.5	-13.8
Daily gradient (°C/day)	1 yr	Avg.	7.3	10.8	11.6	7.7
		Std. dev.	2.9	3.5	3.4	1.6
	50 yr	Ext.	37.1	26.2	27.1	17.7

Figure 2.2 shows the location of the listed towns. The results shown in Table 2.1 revealed remarkably low temperatures in Canada's arctic towns, where average minimum daily temperatures can reach -30°C in winter and extreme cold temperatures

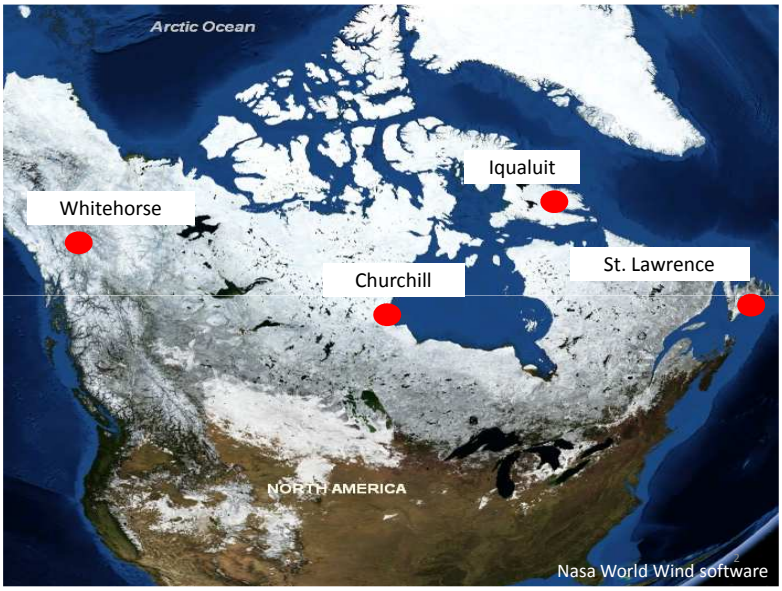

Figure 2.2: Population centres in North Canada with reasonable possibility of wind turbine installation

of -50°C in places such as Iqaluit, Whitehorse and Churchill. These winter average temperatures in Canada are well below the conditions found in Northern and Central Europe and China, where temperatures rarely fall below -20°C [4]. Figure 2.3 shows the monthly variation of temperature and freeze-thaw cycles for Iqualut, Churchill and Churchill. Average temperatures in summer are near 10°C, creating a scenario of high temperature differences between the temperature at which the turbines are likely to be installed and winter temperatures. It is also interesting to note that in places such as Whitehorse, the average number of freeze-thaw thaw-freeze cycles per year is approximately 110 per year.[1] Figure 2.3 depicts the number of freeze-thaw cycles per season.

[1]Freeze-thaw was deemed to occur occurs when a 3-hour temperature record in the time domain (based on data resolution) goes from below zero to above zero; the same for thaw-freeze. Each cycle counted consists of a freeze-thaw plus thaw-freeze event. Thaw-freeze cycles are not expected to occur within the 3-hour temperature record

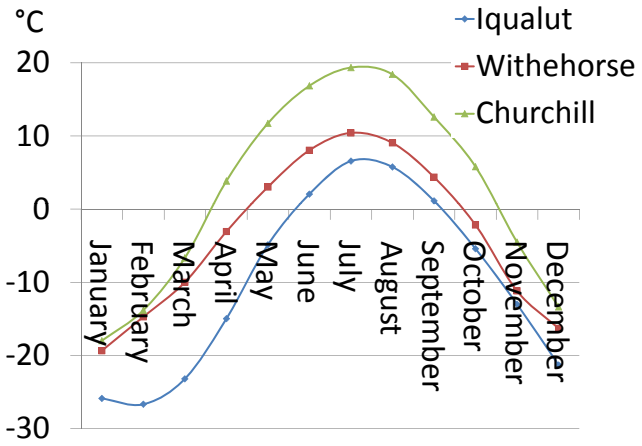

(a) Average daily temperature

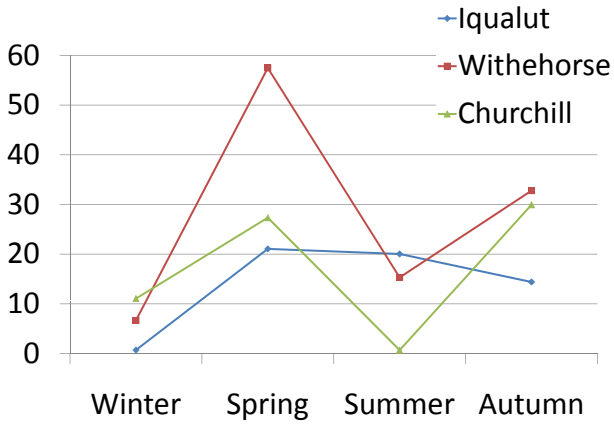

(b) Freeze-thaw cycles per season

Figure 2.3: Climate conditions in Northern Canadian towns

2.2 Nominal Wind Turbine

The wind turbine used throughout this work is based on the WindPACT 1.5 MW Baseline 3-Bladed Turbine (WP1.5MW) described in the WindPACT Turbine Rotor Design Study [37]. This represents a reasonably-sized machine for Northern locations considering transportation and erection logistics. Figure 2.4 obtained from WindPACT study shows a typical blade planform with a linear taper from the maximum chord location (25% r/R) to the blade tip. Figure 2.4 it also indicates a baseline structural arrangement of current commercial blade (25% span station). The primary structural part is a box-spar with webs at 15% and 50% chord and with a build-up of spar cap material between the webs. The exterior skins and internal shear webs are sandwich construction with triaxial fiberglass laminate separated by balsa core.

Aerodynamic and body forces[2] acting on the blade root where obtained using the FAST code[38] from the National Renewable Energy Laboratory (NREL) by means of time-marching simulations. Appendix A extensively details the FAST code. Among others, the FAST inputs used in this work include: active pitch control; all tower, blade and drive train mode DOFs activated; fixed yaw; variable speed control activated. No ice effects were included in the simulations (either mass imbalance or aerodynamic coefficient modifications), as these events occur only around 0°C when there is sufficient moisture, not at the extreme cold temperatures under consideration in the current work. Table 2.2 briefly describes the WP1.5MW configuration. For more details see Appendix B

The wind inflows were obtained from TurbSim [39] which creates three-dimensional and time-varying atmospheric turbulence. This full-field data represents all three components of the wind vector varying in space and time.

The density of the air at room temperature (23°C) is 1.225 kg/m^3 and 1.5 kg/m^3 at -40°C for an atmospheric pressure of 1100 mbar. For this project, shear forces on the root were not considered in the analyses since they are two orders of magnitude lower than the other forces. In the same manner, pitching moments were not included either.

[2]Body forces include gravity and inertial forces; centrifugal forces are included in the inertial forces.

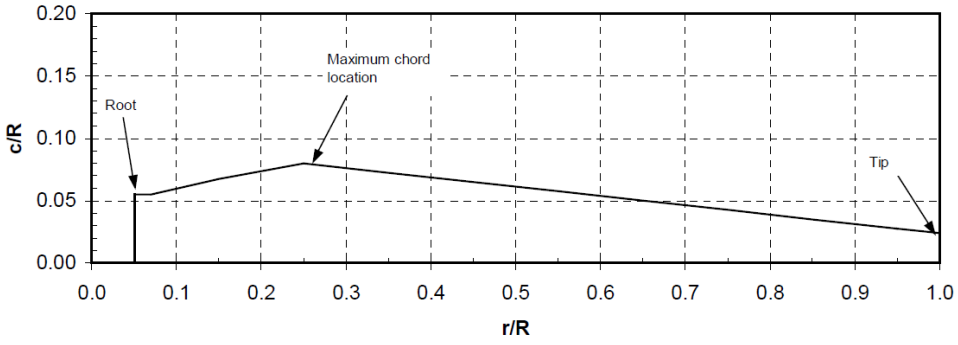

(a) Blade planform

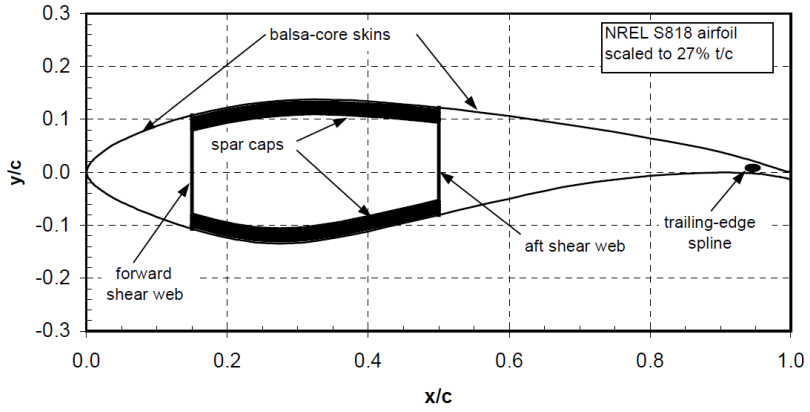

(b) Arrangement of baseline structural model

Figure 2.4: Typical blade structural design. From WindPACT study [37]

Table 2.2: Parameters of the WP1.5MW machine

Rating	1.5 MW
Configuration	3 blades, upwind
Drivetrain	High speed, multiple-stage gearbox
Control	Variable speed and pitch control
Max. rotor speed	20.5 rpm
Blade coning	0°
Rated wind speed	11.8 m/s
Cut-out wind speed	27.5 m/s
Rotor diameter	70 m
Hub height	84 m
Rotor mass	32.02 tons
Nacelle mass	52.84 tons
Tower mass	122.52 tons

2.3 IEC Standards and Safety Factors

For the case of static analysis described in Chapter 3, the extreme hub height wind speeds are defined according to the International Electrotechnical Commission (IEC) Standards, 1999, Second Edition[3], for a Class I turbine. The extreme wind model representing the highest wind velocity in fifty years is described in the IEC standard's equation 6.3.2.1, shown here in Eq. (2.1), where v_{e50} is the 50 year extreme wind speed, v_{ref} is the reference wind speed averaged over 10 minutes (50 m/s for a Class I turbine), z_{hub} is the height of wind turbine hub, and z is the height at which the wind speed is being estimated.

$$v_{e50}(z) = 1.4\, v_{ref}\left(\frac{z}{z_{hub}}\right)^{0.11} \tag{2.1}$$

The Safety Factors (SFs) used in the static analyses were taken from Table 3 of the IEC Standards which give factors for normal and extreme design situations. The safety factor for aerodynamic and operational sources of loading is 1.35. The Germanischer Lloyd (GL) standard states a material safety factor of 2.7 for FRP. The same safety factor was used for the grout. This material safety factor does not

[3]Although newer standards do exist, they were not available to the author and in any case the design cases considered in this thesis remain part of the newer standards and are representative of the design driving cases.

account for the reduction of strength at higher temperatures. A SF of 1.25 was used for the steel.

For the case of fatigue loads, the wind condition was defined according to the IEC standard, case 1.2, Table 2, which indicates a normal turbulence model. It was the only fatigue case considered in this work. Partial safety factor for loads are 1.0 for all normal and abnormal design situations, as stated in section 7.6.3.1 of IEC Standard. The material safety factor for composites in fatigue was defined as 1.93 according to Burton [24].

Chapter 3

Static Analysis

This chapter analyzes blade root connections subject to extreme limit loads in cold conditions using a FE approach. The two most common connector types used in the industry are studied: embedded carrots and T-bolts. First, a material database is developed based on experimental information and composite micromechanics theory. Later, the extreme loads acting on the blade root connections from extreme winds are estimated. Then, extreme thermal loads as seen in Canadian Northern climates are applied. Finally, static failure is analyzed in detail around the root connection and surrounding areas according to maximum strain, maximum stress, Tsai-Hill and Hashin (decomposed) criterion.

Fatigue analysis of the entire blade is detailed in Chapter 4. The emphasis in the current chapter is on a detailed investigation of possible thermally-induced stresses around the structural details of the root connections under extreme loading conditions. It was anticipated that combined static and thermal loading of these connections were the most relevant potential failure modes to study.

3.1 Blade Root Connection Types

Composite blades are connected to metallic cast hubs and pitch bearings by metallic connections. Fig. 3.1 shows a Nordex 40 m length blade being installed at Scout Moor Wind Farm in England. The metallic connections at the root of the blade are clearly visible.

Generally, the connection are so-called 'carrots' embedded in the blade root, which in turn are attached to the bearing ring by a bolt, as shown in Fig. 3.2a. The metallic

Figure 3.1: Installation of wind turbines at Scout Moor Wind Farm, England. Source: Wikimedia commons: www.wikimedia.org

carrot faces bear on the pitch ring, and bolt pre-loading primarily creates stresses in the embedded carrot. Instead of carrots, bolt studs may be embedded in the root, as in the blade in Fig. 3.1; these connections function similarly to carrots although the composite face becomes the bearing surface.

Some manufacturers laminate the embedded carrots directly into the blade during the manufacturing process, while others drill holes and bond the connection during assembly [40] . Direct insertion reduces the manufacturing time but requires exceptional care during cure. The alternative is to drill holes and bond the inserts with an epoxy grout. Embedded carrots result in a smooth load transfer between the composite root and the hub. One disadvantage of this connection however is the high cost of threaded inserts and the difficulties associated with bonding, for example the presence of discontinuities like air bubbles in the grout/steel contact. Vestas, the largest worldwide manufacturer of wind turbines, uses embedded carrots in several of their designs.

An alternative configuration to carrots are T-bolts, shown in Fig. 3.2b. In T-bolt connections, bolts passes through the pitch bearing ring, into axial holes in the blade skin and are tightened into pins passing transversely through the blade skins. The composite blade root bears directly on the metallic pitch ring, and bolt pre-

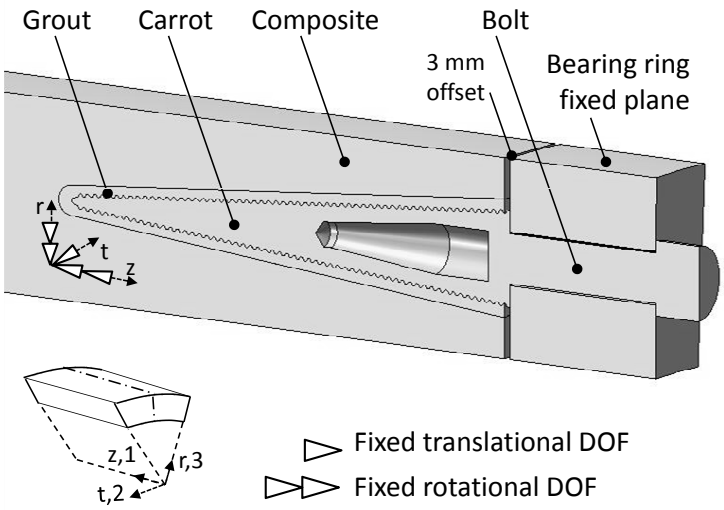

(a) Carrot

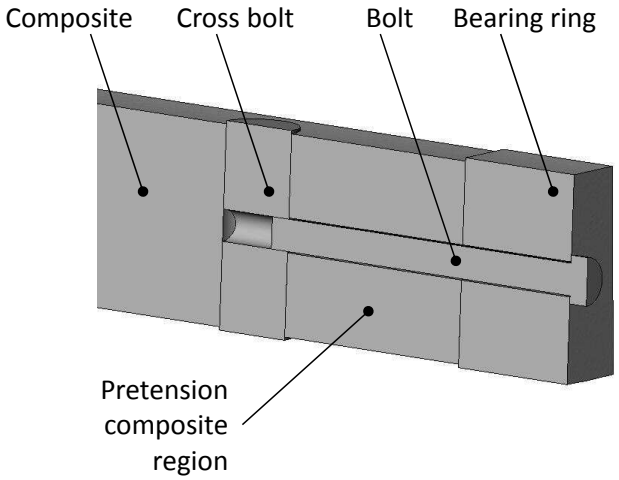

(b) T-bolt

Figure 3.2: Single connection model

loading stresses the material in the composite root directly. GE Energy blades use this configuration.

Over the last several years T-bolt designs have become more popular in new blade designs due to their low manufacturing costs as compared to threaded inserts. Also, a T-bolt connection does not rely on adhesives, and more importantly, damaged studs or barrel nuts can be removed and replaced. However, T-bolt connections create a highly stressed region on the composite blade around the cross bolt. T-bolts also need high drilling accuracy to prevent bending of root stud. For larger blades, multiple rows of T-bolts may be used to better distribute stresses through the composite and over a greater number of bolts.

The number of bolts for the blade root analyzed in this study was obtained from the blade-scaling study document released by NREL [41]. From that reference, for a standard machine of 1.5 MW and a blade root of 1.75 m diameter, the number of bolts recommended was 50.

3.2 Connection Loads

The result of the dynamic wind turbine simulations are net time varying bending moments $M(t)$ and axial forces acting on the blade root, which generate axial forces on the bolts in the connection system. Figure 3.3 shows the moment-force system acting on the root (where x and y represents the edgewise and flapwise axis respectively. This coordinate system pitches with the blade). Note that near bolt j the joint is subject to compression whereas near bolt i the connection is under tension. Since the total net bending moment acting on the root for a given time is equivalent to the moments generated by the connection bolt's axial forces, we have that:

$$\left|\vec{M(t)}\right| = \sum f_i(t) d_i(t) \tag{3.1}$$

where t is time, $M(t)$ is the total net bending moment acting on the blade root for a given time and contained in the $x - y$ plane, $f_i(t)$ is the equivalent axial force transmitted to the i^{th} bolt, and $d_i(t)$ is the minimal (perpendicular) distance from the i^{th} bolt to the net bending moment axis.

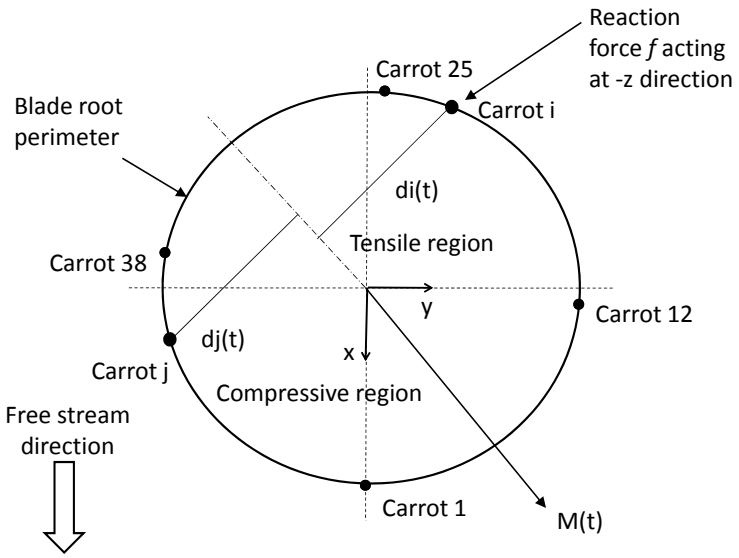

Figure 3.3: Distribution of loads on blade root connections

If we assume that reaction forces f are proportional to the distance d[1], then:

$$f_i(t) = h(t)d_i(t) \tag{3.2}$$

where $h(t)$ the constant of proportionality. Now substituting Eq. (3.2) into Eq. (3.1) allows us to find $h(t)$ as:

$$h(t) = \frac{\left|\vec{M(t)}\right|}{\sum d_i(t)^2} \tag{3.3}$$

Therefore, using $h(t)$, the reaction forces at each bolt can be obtained. The reactions are compressive and tensile forces according to the side on which the bolts are located relative to the total bending moment vector acting at a given time. Finally, the total axial force acting on the connection (denoted the connection axial load) is equal to the equivalent force due to bending moments described above, plus the axial forces obtained from FAST and assumed distributed equally between all bolts. This assumption was tested with a 3-D finite element model of a full blade root. The

[1]This assumption is consistent with standard linear beam cross-section theory, and was validated through the use of the full-blade FE presented in Chapter 4.

results showed that the distribution of bolt loads determined by Eq. (3.3) is in fact valid and accurate.

Table 3.1 shows the maximum bolt axial loads registered in the blade root for the WP1.5MW turbine under different wind (cut-out wind speed, the maximum speed for 1 year return period, maximum wind speed for a 50 year return period), temperature (room and extreme) and operational (operational and parked) conditions. The extreme hub height wind speeds are defined according to the International Electrotechnical Commission (IEC) Standards, 1999, Second Edition, for a Class I turbine. Eq. (2.1) shows the Extreme Wind Model (EWM) used. Reference velocity is defined as 50 m/s and the hub height is 84.3 meters. This results in a extreme wind of 70 m/s (252 kph) at hub height. The load SF applied to these results for the analyses in the following sections is 1.35 (not included in Table 3.1). Both tensile and compressive forces in each case have the same magnitude.

Table 3.1: Maximum connection axial load registered in the blade root connections for the 1.5MW WindPact turbine [KN]

	Room temp (23°C)		Cold temp (-40°C)	
Wind speed	Operational	Parked	Operational	Parked
Cut-out (27.5 m/s)	70	40	66	48
V_{e1} (52 m/s)		124		144
V_{e50} (70 m/s)		216		251

In general, the fully reversed direct gravitational force and steady centrifugal direct axial loads account for just a small part of the axial load applied to the bolted connections.[2] Most of the axial load carried by the bolts is being caused by the bending moments. The proportion depends on the location of the connection around the root diameter, since connections located far from the axis of the moment vector take more load than connections on the moment axis.

For the case of the connections taking most of the moment, on average the bending moments are causing almost 90% of the axial load. Table 3.1 shows that the total connection axial loads at the cut-out wind speed of an operating turbine are higher than for a parked turbine at the same wind speed. Since as stated the direct axial root forces account for a small part of the connection axial load, this increment is due

[2]The reversed gravitation load becomes relatively more important for larger blades.

to the higher bending moments of the operating turbine. Additionally, the connection axial load of a turbine working at room temperature is slightly higher than the load for a machine operating at -40°C. This is due to the opposing effects of the pitch control and the change of air density that overall reduces the flapwise bending moments and increases the edgewise moment at cold temperatures. Finally, Table 3.1 shows that for a parked turbine (in which the pitch control is inactive) the difference in the connection axial load is almost proportional to the change in air density.

These results were used to define the cases to evaluate the performance of the connection systems by means of a FE model at extreme cold temperatures considering static and ultimate load scenarios.

3.3 Finite Element Model

The FE model treats the composite structure as a homogenized material with orthotropic properties. Therefore, this macro scale FE analysis considers the composite at a laminate level and does not model the micro constituents of the composite (fiber, matrix, interface) or single plies (lamina). This simplification is consistent with the experimental data at room and cold temperature obtained by the authors collaborators working with composite coupons, which can be considered as laminate scale data. The work here considers the effect of microscale phenomena occurring in the composite laminate. This approach inherently includes singularities and discontinuities created during composite manufacture and the complex mechanical interaction of composite constituents.

The FE model was assembled and modelled in ANSYS Workbench and ANSYS. The FE model is predominantly based on 20 node hexahedral 3-D elements with 3 translational degrees of freedom in the x, y, and z directions at each node (60 DOF in total). Since the focus of this work is the composite and grout areas and interfaces, the steel carrot, pitch bearing and the bolt were modelled with less complex elements, mainly tetrahedrons. Solid elements have been satisfactorily implemented in other works analyzing thermal and mechanical stresses in steel surfaces bonded to FRP materials [33]. Hexahedral 3-D elements were used for embedded carrot and T-bolt root design in the static analysis since it is difficult to match layered elements with the root/bolt geometry. For dynamic analyses the whole blade including the root was modelled with layered elements. See Chapter 4. Finally, the different volumes

representing the parts of the blade root section were merged in the FE model in order to reduce the presence of contact surface elements. The composite material in the FE model is E-glass/epoxy with unidirectional fibres aligned with the blade pitch axis.

Layered solid elements were not used in the case studies presented in this thesis, as the root is predominantly made up of uni-axial material. To test this assumption, a number of alternate FE models were constructed incorporating regions of ± 45 °off-axis fibres on the inner and outer skins of the root. The results did not show any significant changes in the stress distributions, so the simplified uniaxial material models were used for the remainder of the study. In any case, further experimental testing would have been required to verify the strength properties of ply layups incorporating off-axis fibres.

In the carrot connection, an epoxy grout (adhesive) glues the steel carrot to the composite root section. Figure 3.2a shows the carrot connection. As seen in Fig. 3.2b a T-bolt connection has a transverse bolt which transmits the forces between the composite laminate and a pretensioned spanwise bolt.

Figure 3.2a depicts the boundary conditions for the FE model indicating also a radial, tangential and axial coordinate system (r, t, z) representing the root blade geometry and also a fibre-orientated coordinate system $(1, 2, 3)$. Due to symmetry, the FE model treats the connection system as a half-model of a single connection and surrounding composite. The variation in loading between adjacent connections is very small, validating treating the connection as symmetric through the axis of the bolt. As boundary conditions, the outer face representing the pitch bearing race is defined as a fixed support. A cross-section plane outboard on the blade, parallel to and far from the hub-root connection plane, is assumed to receive the pressure representing the loads applied to the blade root section. That plane allows displacements in the tangential and radial direction, and in order to not disturb stress results near the hub-root connection must be away from the bearing ring/root interface. For this project the outward plane was located 1 m from the bearing ring to minimize the effect of the applied pressure surface distribution on the hub/blade region. The planes of symmetry (the sides of the model through the composite shell and through the connection) are allowed to displace in the axial and radial directions but are constrained in the tangential direction. They can also rotate in-plane but not out-of-plane to satisfy the symmetry conditions.

It is important to note that in the carrot connection, the composite face of the

blade does not touch the pitch bearing. To respect this, the composite has a small offset relative to the carrot mating surface, i.e. it is the connection and not the composite blade surface which transmits the mechanical loads between the blade and the hub. The T-bolt connection is modeled quite similarly, except that the composite bears directly on the pitch bearing surface. Contact surface elements were included in that contact area and in the cross-bolt hole with a friction coefficient of 0.2 (polymeric composite on steel). All the models ignore the details of the threads on the bolts, instead assuming stress transfer in the first few threads by implementing rigid connections. This interactive stress area of the bolt-carrot and bolt-cross bolt system is defined as half of the diameter of the respective bolts.

The dimensions of the various components in the blade root assemblies were designed to provide adequate performance at conventional room-temperature design conditions, and to be representative of realistic blade designs. The diameter of the blade in the root region is 1.75 m with a skin thickness of 10.5 cm for the carrot connection and 15 cm for the T-bolt connection. The grout in the carrot connection has an average thickness of 5 mm and a smooth grout/composite interface. The embedded tapered carrot is 30 cm long with a external diameter of 31.5 cm. The modeling of the surface of the carrot includes grooves of 1.5 mm radius which enhance the fixing of the carrot in the epoxy glue. This detail is typical of commercial carrots, and was taken to be similar to a commercial propriety carrot design supplied in confidence to the author.

The bolt preload of the carrot bolt is 75% of its proof strength, which for the case of the M30 Class 12.9 bolts used here equals 219 KN. The T-bolt connection uses a M24 lengthwise bolt with a 85% pretension which is recommended for static loads and represents a worse case in terms of compressive stresses acting in the composite region. Also, this pretension was designed to keep the blade root from separation under ultimate tensile loads. The cross bolt is 6 cm in diameter and is located 19 cm from the ring hub/root interface. The pitch bearing is 10 cm thick for both types of connection.

Several mesh sizes where evaluated to check the convergence of the FE model. The results showed little variation of stress magnitude in the critical areas of the connection above 100,000 elements. The size of the mesh was chosen considering computational resources and time simulation. The final FE model contains over 150,000 elements with good resolution through the blade skin thickness.

With respect to the stresses included in the FE model, the different parts of the connection system and the bonded joints consider: a) the mechanical stresses, and b) the residual stresses due to thermal stresses for a reference temperature of 23°C. Thus, the curing and any post-curing stresses due to chemical and physical changes of the adhesive in the carrot connection are considered insignificant compared with the other stresses [42]. Also, for the extreme cold temperature cases, thermal equilibrium is assumed so that there are no stresses caused by a non-uniform distribution of temperature. Finally, the FE model does not consider the residual stresses in the micro scale between the fibre, the matrix and the interface, which are assumed to be included in the tested composite coupons.

3.4 Static Material Properties

There is not much available information on composite properties at the cold temperatures seen in Canada. In fact, current procedures recommend full shutdown when temperatures drop below -30°C [43], an operational curtailment that is too restrictive for Canadian operations to become more widespread. The composite parameters used here were primarily obtained from a material testing program conducted by collaborating specialists Comier and Joncas *et al.* at ETS in Montreal [5]. Their campaign has to date tested a series of uniaxial E-glass/epoxy coupons with a fibre volume fraction of 55% at -40°C. The same V_f for the blade was assumed in this work.

An exhaustive literature review on composite properties under temperature cycling, hygrothermal conditions and cold temperatures was also undertaken. An important source of information on composite properties under normal environmental conditions is the testing program carried out by Mandell and Samborsky [8] and sponsored by Sandia National Laboratories in the USA. When not available from the ETS experimental test campaign, the properties of the composite for extreme cold temperatures were assumed considering micromechanics and matrix/fibre predominance. Table 3.2 shows the engineering properties for materials used to model the connections in the FE model.

The carrot and bolts of the connections are made of steel and the properties of the grout gluing the embedded carrot are assumed to be similar to epoxy. Engineering properties, Coefficient of Thermal Expansion (CTE) and strength of the epoxy grout for room and extreme cold temperatures were obtained from Choi [13]. Poisson's ratio

Table 3.2: Material properties at room and extreme cold temperature

	23 °C			-40 °C		
	FRP	Grout	Steel	FRP	Grout	Steel
E_1 [MPa]	40,200	3,100	200,000	41,491	4,400	200,000
$E_{2,3}$ [MPa]	10,057			13,074		
$\nu_{12,13}$	0.256	0.35	0.30	0.308	0.40	0.30
ν_{23}	0.274			0.308		
$G_{12,13}$ [MPa]	5,667	1,222	76,923	7,219	1,571	76,923
G_{23} [MPa]	3,948			4,998		
CTE_1 [10^{-6}/°C]	7	56	12	7	48	12
$CTE_{2,3}$ [10^{-6}/°C]	23			23		
SF	2.7	2.7	1.25	2.7	2.7	1.25
σ_1^T, σ_Y [MPa]	392	51	760	461	57	760
σ_1^C [MPa]	235			259		
$\sigma_{2,3}^T$ [MPa]	11			12		
$\sigma_{2,3}^C$ [MPa]	48			53		
$\tau_{12,13}^F$ [MPa]	19			25		
τ_{23}^F [MPa]	7			7		

was assumed as 0.35 for room temperature and 0.4 for extreme cold conditions. The engineering properties of steel were assumed as standard and linear with temperature for a high strength steel.

For the composite at room temperature E_1 and ν_{12} were obtained directly from Cormier [5].E_2 for V_f=55% was estimated according to Eq. (3.4) defined by Samborsky [8] to extrapolate from experimental data, where E_2^* indicates the transverse modulus at the 0.45 fibre volume fraction for the composite UD D155 available in Samborsky's database.

$$\frac{E_2}{E_2^*} = \frac{1}{2.206} \frac{1 + 0.036\, V_f}{1 - 0.836\, V_f} \tag{3.4}$$

ν_{23} and G_{23} for V_f=55% were obtained by linearly extrapolating from experimental data for UD D155 composite available in Samborsky with V_f=36% and V_f=44%.

G_{12} at room temperature was estimated according to Eq. (3.5) defined by Samborsky [8] to extrapolate from experimental data, where G_{12}^* indicates the shear modulus at the 0.45 fibre volume fraction for composite UD D155.

$$\frac{G_{12}}{G_{12}^*} = \frac{1}{2.809}\,\frac{1 + 1.672\,V_f}{1 - 0.836\,V_f} \tag{3.5}$$

Transverse isotropy was assumed so that $E_2 = E_3$, $\nu_{23} = \nu_{13}$, $G_{13} = G_{12}$, $\sigma_2^T = \sigma_3^T$, $\sigma_2^C = \sigma_3^C$, and $\tau_{12}^F = \tau_{13}^F$.

For uniaxial composite properties at cold temperatures some assumptions were made. E_1 was measured by Cormier and E_2 was increased by 30% with respect to room temperature. That percentage is the change in E_2 predicted by the rule of mixtures between 23°C and -40°C. In this work E_2 was obtained by extrapolating from the experimental data as described above. An alternative method is to obtain the modulus by micromechanics as stated in Eq. (3.6) using epoxy and E-glass properties to obtain perpendicular-to-fibre modulus [11]. Data for E-glass and epoxy at different temperatures was obtained from [13] and [14], and it was assumed that E-glass fibre keeps its properties at -40°C. The material data it is summarized in Table 3.3

$$\frac{1}{E_2} = \frac{V_f}{E_{fibre\ glass}} + (1 - \frac{V_f}{E_{epoxy}}) \tag{3.6}$$

Table 3.3: Epoxy and E-glass engineering properties at different temperatures

	23°C	-40°C
E_{epoxy} [Mpa]	3100	4400
ν_{epoxy}	0.35	0.40
G_{epoxy} [MPa]	1222	1571
$E_{fibre\ glass}$ [Mpa]	72400	72400
ν_{epoxy}	0.2	0.2
G_{epoxy} [MPa]	30200	30200

Micromechanic estimation (also known as the rule of mixtures) results in a value of $E_2 = 6.54$ GPa at room temperature for the unidirectional composite used here, much lower than the 10.06 GPa predicted by Eq. (3.4). The value obtained from the micromechanic relationship was considered too low, however micromechanics was used to predict the change in Young's modulus at cold temperatures. Using micromechanics, the transverse Young's modulus E_2 goes from 6.57 GPa at room temperature to 9 GPa at -40°C, 37% higher. Consequently, a factor of 30% representative of that

increment was used in this work, increasing E_2 from 10.057 GPa at room temperature to 13.074 GPa at cold temperatures.

ν_{12} was also measured by Cormier and equals 0.328 with a standard deviation of 0.2. In order to be consistent with other low temperature properties used in this work (recall that E and G and ν cannot be independently specified) a Poisson's ratio of 0.308 was employed which falls in the range of values predicted by Cormier. The same value was assumed for ν_{23}.

E_2 and G_{12} at cold temperatures were also scaled from room temperature using the increment predicted by the rule of mixtures. The rule of mixtures estimates a G_{12}=3.42 GPa at room temperature according to Eq. (3.7) [11]. At cold temperatures, micromechanic predicts G_{12}=4.31 GPa, a difference of 26%. Therefore, a factor of 26% was used to increase G_{12} from 5.66 GPa estimated by Eq. (3.5) to 7.21 GPa at cold temperatures. G_{23} at cold temperatures was increased by the same factor of 27%.

$$\frac{1}{G_{12}} = \frac{\frac{V_f}{G_{fibre\ glass}} + 0.6\ \frac{1-V_f}{G_{epoxy}}}{V_f + 0.6\ (1 - V_f)} \tag{3.7}$$

For room temperature, σ_1^T, σ_1^C, and τ_{13}^F of the composite were obtained directly from Cormier. The tensile strength in the transverse direction σ_2^T was obtained from Samborsky linearly extrapolating from experimental data for UD D155 composite with V_f=36% and V_f=44%.

The compressive strength in the transverse direction σ_2^C was also obtained from UD D155 and assumed the same as FRP with V_f=44%, since compressive strength are typically to be less sensitive to V_f in the transverse direction.

At cold temperatures, σ_1^T, σ_1^C, and τ_{13}^F of the composite material were obtained directly from Cormier. As can be seen in Table 3.2 the increase in the strength is 18% and 10% for σ_1^T and σ_1^C respectively, and 27% for τ_{13}^F. From that information, the rest of the strengths in the transverse direction were assumed to increase by a conservative 10%.

Finally, the SF for the FRP and the grout is 2.7 and does not account for the reduction of strength at higher temperatures according to GL standards. A SF of 1.25 was used for the steel.

The CTE at room temperature for the composite was defined according to data reported by Hyer [11] and Kaw [12]. Hyer states that epoxy/glass composite with

similar V_f has a CTE=23.3 $\times 10^{-6}/^{\circ}$C in the perpendicular-to-fibre direction and 6.34 $\times 10^{-6}/^{\circ}$C in the fibre direction. Kaw depicts CTE as function of V_f stating a CTE of 18 $10^{-6}/^{\circ}$C and 7 $10^{-6}/^{\circ}$C for perpendicular-to-fibre and fibre directions respectively for V_f=55% . Finally, CTE_2=23 $\times 10^{-6}/^{\circ}$C and CTE_1=7 $\times 10^{-6}/^{\circ}$C were used in this work at room temperature.

As before, the rule of mixtures was used to estimate the change in CTEs at cold temperatures. Micromechanical composite models of CTE stated in Eq. (3.8) and Eq. (3.9) [11] predict very low variation between 23°C and -40°C, so the same values of CTE for the composite were used for extreme cold and room temperatures.

$$CTE_1 = \frac{CTE_{fg}\ E_{fg}\ V_f + CTE_e\ E_e\ (1 - V_f)}{E_g\ V_f + E_e\ (1 - V_f)} \tag{3.8}$$

$$\begin{aligned} CTE_2 =& CTE_e + ((CTE_{fg} - CTE_e)V_f + \\ & (E_{fg}\nu_e - E_e - E_e\nu_{fg})(CTE_e - CTE_{fg})(1 - V_f)V_f)/E_1 \end{aligned} \tag{3.9}$$

where the subscripts f, g, e and g indicates fibre-glass, epoxy and glass associated properties respectively.

3.5 Failure Criteria

Failure in composite materials is defined in the same manner as for isotropic materials; a composite piece fails when it loses its capability to carry its designed load. Composite materials are much more complex due to their composition and the strong asymmetry caused by the presence of fibres, whose longitudinal strength is several times larger than the matrix strength. It is clear that the orientation of the fibres determines the performance of the composite. Tensile strength in the fibre direction is controlled by fibre properties whereas tensile strength perpendicular to the fibre orientation is determined by the polymer matrix properties and the fibre-matrix bond. Analogously, the composite's strength in any other direction is a function of the angle relative to the fibres. Even though these facts are well known, there is still controversy around composite failure theories since no single methodology fits the data perfectly in all situations [11].

Failure of composites is the result of several mechanisms acting concurrently. The matrix could be subject to yielding or may be degraded by brittle cracking, fibres breaking or separating from the matrix, or fibres buckling under compressive forces. All these mechanisms deteriorate the condition and efficiency of how the stress is transferred between fibre and matrix. Moreover, a typical composite structure is made of various layers with different fibre orientations and discontinuities due to manufacturing processes, adding extra complexity to failure estimation. Therefore, appropriate failure theories for fibre-reinforced composite materials are still an active research field.

In general, standards for wind turbines blade design recommend analyzing composite performance according to more than one methodology and at both the laminae and laminate level. For example, the DNV standards [17] contain a detailed description of criteria for composites, suggesting, among others, the maximum stress and maximum strain criterion, Tsai-Wu and Tsai-Hill criterion, cracking interaction method, and in-plane shear failure. The DNV standard also recommends analyzing the composite structure at the individual ply level. For the uniaxial composite under investigation, the interlaminar failure mechanism is of less importance that it is for woven fabrics.

According to a US FAA report [16], the most used criteria among researches and specialists are the maximum strain, maximum stress, Tsai-Wu, Tsai-Hill and Hashin criterion. The first two methods do not consider interaction among stress and strain conditions. The Tsai-Wu is an interactive composed criteria that requires the determination of an experimental parameter relating failure in the fibre direction and transverse stress. The Tsai-Hill is an single integrated interactive criterion which is an extension of the von Mises yield criterion to orthotropic materials [18]. The additional experimental parameter required for the Tsai-Wu criteria was unavailable for the composites considered in the current work. The Hashin criteria considers decomposed failure modes defining separate formulations for matrix and fibre failures. Christensen [20] states that decomposed forms are suitable for highly anisotropic materials whereas non-decomposed forms apply near the isotropic conditions. According to Christensen, high anisotropy occurs when $E_2/E_1 \leq 0.1$, $\sigma_1^T/\sigma_2^T \gg 1$, and $\sigma_1^C/\sigma_2^C \gg 1$. For the case of the epoxy/E-glass composite analyzed here the values are 0.25, 40 and 4.8 respectively. Evidently, for the FRP used in this study, the composite's strength is quite orthotropic, but not the Young modulus. This implies that the composite

failure analysis should formally include both integrated and decomposed criteria.

Since the objective of this work is not to obtain an optimal connection design, but rather to analyze the role of thermal and mechanical loads at extreme cold temperatures, the criteria considered here are good indicators of stressed zones and help to explain the mechanism and interaction of the blade root constituents, rather than serve as exact indicators of failure. In order to compare the different stressed areas this work includes maximum strain, maximum stress, Tsai-Hill and Hashin (decomposed) criteria. Failure is considered to occur when one of the elements fails according to a lamina criterion and does not consider a progressive damage criterion.

Equation (3.10) and Eq. (3.11) show the maximum strain criterion, where i=1,2,3 and (p,q)=(1,2),(2,3),(3,2). Equation (3.12)and Eq. (3.13) show the maximum stress criteria. Equation (3.14) shows the Tsai-Hill criterion for the tensile mode [3]. The Hashin criterion is decomposed according to the failure mechanism. Equation (3.15) shows tensile matrix mode, Eq. (3.16) shows compressive matrix mode, Eq. (3.17) shows tensile fibre mode, and Eq. (3.18) describes compressive fibre mode [16].

$$\frac{\sigma_i^T}{E_i} > \epsilon_i > \frac{\sigma_i^C}{E_i} \tag{3.10}$$

$$\frac{\tau_{pq}}{G_{pq}} > |\epsilon_{pq}| \tag{3.11}$$

$$\sigma_i^T > \sigma_i > \sigma_i^C \tag{3.12}$$

$$\tau_{pq} > |\sigma_{pq}| \tag{3.13}$$

$$\begin{aligned}&\frac{\sigma_1^2}{\sigma_1^{T^2}} + \frac{\sigma_2^2}{\sigma_2^{T^2}} + \frac{\sigma_3^2}{\sigma_3^{T^2}} + \frac{\tau_{12}^2}{\tau_{12}^{F^2}} + \frac{\tau_{13}^2}{\tau_{13}^{F^2}} + \frac{\tau_{23}^2}{\tau_{23}^{F^2}} - \sigma_1\sigma_2\left(\frac{1}{\sigma_1^{T^2}} + \frac{1}{\sigma_2^{T^2}} + \frac{-1}{\sigma_3^{T^2}}\right)\\ &-\sigma_1\sigma_3\left(\frac{1}{\sigma_1^{T^2}} + \frac{-1}{\sigma_2^{T^2}} + \frac{1}{\sigma_3^{T^2}}\right) - \sigma_2\sigma_3\left(\frac{-1}{\sigma_1^{T^2}} + \frac{1}{\sigma_2^{T^2}} + \frac{1}{\sigma_3^{T^2}}\right) < 1\end{aligned} \tag{3.14}$$

[3]The dominant stresses acting on the material defines the strength used in the formulation; tensile or compressive

$$\frac{1}{\sigma_2^{T\,2}}(\sigma_2+\sigma_3)^2+\frac{1}{\tau_{23}^{F\,2}}\tau_{23}^2-\sigma_2\sigma_3+\frac{1}{\tau_{12}^{F\,2}}\tau_{12}^2+\tau_{13}^2<1 \tag{3.15}$$

$$\frac{1}{\sigma_2^C}\left(\left(\frac{\sigma_2^C}{2\tau_{23}^F}\right)^2-1\right)(\sigma_2+\sigma_3)+\frac{1}{4\tau_{23}^{F\,2}}(\sigma_2+\sigma_3)^2+\frac{1}{\tau_{23}^{F\,2}}(\tau_{23}^2-\sigma_2\sigma_3)+\frac{1}{\tau_{12}^{F\,2}}(\tau_{12}^{F\,2}+\tau_{13}^{F\,2})<1 \tag{3.16}$$

$$\left(\frac{\sigma_1}{\sigma_1^T}\right)^2+\frac{1}{\tau_{12}^{F\,2}}(\tau_{12}^2+\tau_{13}^2)<1 \tag{3.17}$$

$$\left(\frac{\sigma_1}{\sigma_1^C}\right)^2<1 \tag{3.18}$$

3.6 Results

This section discusses the results from the various static root connection models.

3.6.1 Carrot Connection

Carrot with Thermal Load Only

The first FE model analyzes a carrot connection under a thermal load of -63°C produced by going from room temperature (23°C) to -40°C. The reference temperature is 23°C since the carrot is embedded in the blade root by drilling and gluing the carrot once the composite has cured.[4] This first case does not consider any aerodynamic loads, to show the magnitude and characteristic of thermal stresses. Also, this work assumed uniform temperature distribution for simplification.

Figure 3.4 shows the failure criterion value corresponding to the thermal load on the carrot connection. The Tsai-Hill value is shown in the composite regions, and the von Mises criteria for the orthotropic materials (steel and epoxy grout). The interface of the grout along the carrot and the base of the blade are the most affected regions due to thermal stress, especially the end of the carrot and the plane indicated as section α. The sharp end of the carrot is affected by the high mismatch between

[4]Co-cured carrots, in which the carrot is laid up and infused at the same time as the blade structure, may develop even higher effective loads owing to the exotherm of the composite during curing

the low CTE of the composite in the fibre direction and the relatively high CTE of the grout and the steel. At low temperatures, the carrot trends to shrink more than the composite in the fibre direction, creating a high strain constraint.

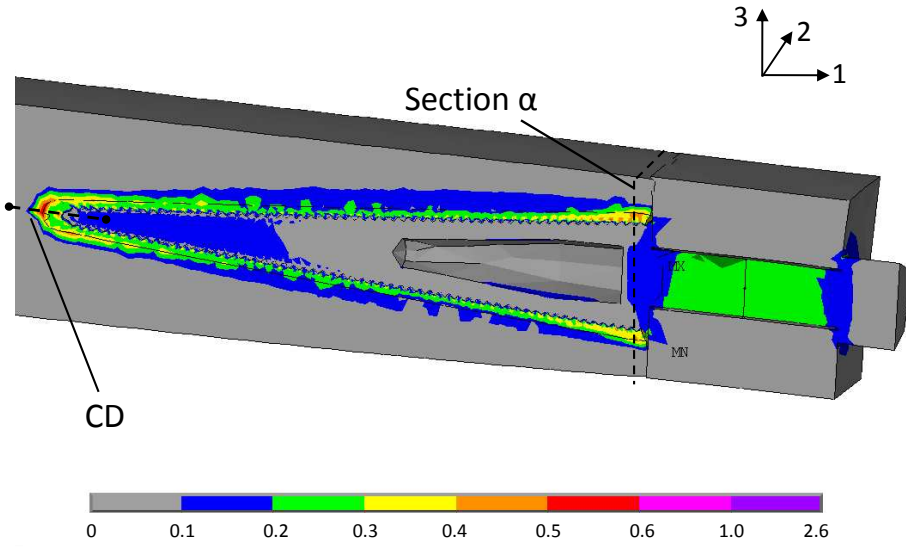

Figure 3.4: Tsai-Hill criterion and σ_{vm}/σ_Y ratio in a carrot subject to thermal load

Figure 3.5 depicts the transverse stress σ_2 through section α (indicated in Fig. 3.4) which represents a plane close to the blade base. It can be seen that the zone at the base of the carrot is affected by the hub bearing ring boundary condition (fixed) constraining the large shrinking deformation of the composite in the 2-direction, in turn creating a tensile stress σ_2, which is matrix governed and with a low tensile strength of 12 MPa. Figure 3.5 also shows a strong stress gradient in the interfaces between the steel, grout and composite. These variations in the stresses are expected in bi-material interfaces.

Figure 3.6 depicts the stresses through line AB indicated in Figure 3.5 which represents a path crossing through the middle of the blade root thickness. The fibre-orientated directions (1, 2, and 3) in the orthotropic materials represent an arbitrary coordinate system and are depicted to show the stress variations. The same is valid for the von Mises stress in the composite region. It is seen in Fig. 3.6 that all the stresses

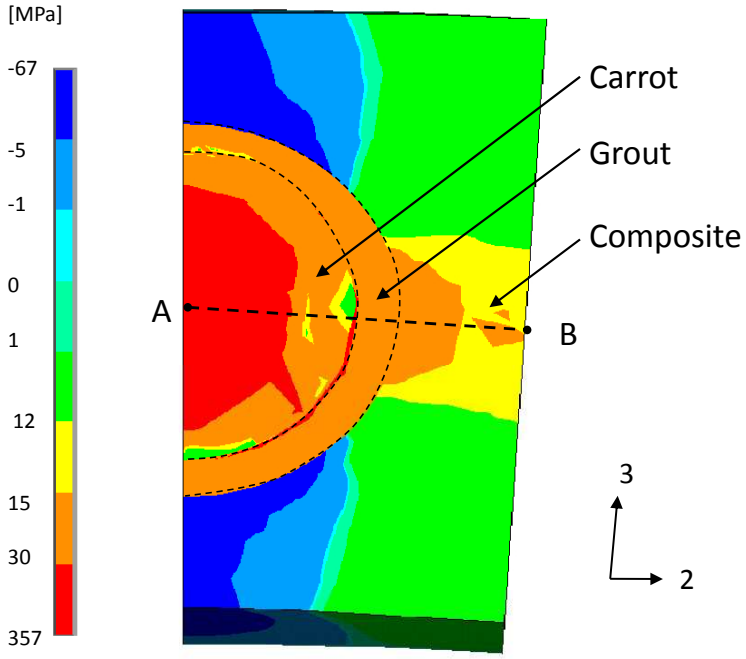

Figure 3.5: Distribution of the stress perpendicular to fibre (σ_2) in carrot section α near the hub/blade connection (note scale is not uniform)

are extremely variable, especially across the grout due to the complex interaction among the constituents of the blade root caused for the thermal load of 63°C.

Figure 3.6a shows that the von Mises σ_{vm} stress in the steel is much higher than in the grout due to its higher Poisson's ratio, but is well below its yield strength. The von Mises stress of the grout has a maximum of 39 MPa, again below its yield strength of 57 MPa for cold temperatures. Figure 3.6a also shows that σ_1 acting in the composite is in the range of -5 MPa and 10 MPa, well below the respective strengths. In the transverse 2-direction the composite is shrinking significantly due to its high CTE in that direction, creating a tensile condition propagated through the hub/blade connection region. As can be seen, the tensile thermal transverse stress in the 2-direction is in the order of 17 MPa. Thus σ_2 is causing failure under the maximum stress criterion since σ_2^T is equal to 12 MPa at -40°C (assuming a SF of 2.7 for composite strengths). Failure for composites under tensile stresses acting perpendicularly to the fibre direction (σ_2 or σ_3) is due to tensile failure of the matrix, failure at the bond between fibre and matrix, or failure trough fibre diameter. In

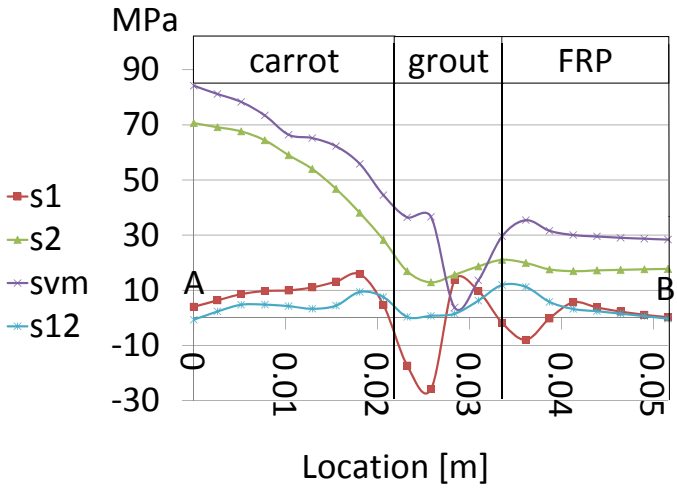

(a) Stresses in a fibre-orientated coordinate system and σ_{vm}

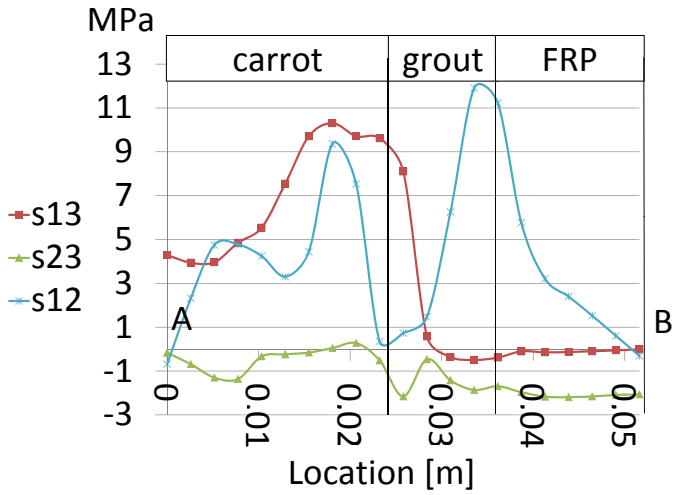

(b) Shear stresses in a fibre-orientated coordinate system

Figure 3.6: Stresses in a section at the base of the carrot (path AB) due to a thermal load of 63°C

addition, Table 3.4 shows the contribution of each term of the 2D Tsai-Hill formula along the path from A to B in the composite region. σ_3 is not shown in these calculations as it is negligible.

It can be seen that the tensile transverse stress σ_2 is primarily responsible for the failure status predicted by the Tsai-Hill criterion. There is also a small contribution to failure near the grout interface due to σ_{12}, but it is one order of magnitude smaller than the contribution of σ_2.

The interactive term that relates the fibre and transverse stresses is not significantly contributing to reduce the failure status. The negative sign and the magnitude of the interactive term point to the fact that a tensile stress in the 2-direction is slightly reducing the contribution from σ_2. Additionally, σ_3 (not shown in the table) has a compressive state (well below σ_3^C) and is not contributing to decrease the strain caused by σ_2. It is important to notice that the FE model presented here does not consider the presence of a random mat in the shell structure. A number of additional FE models with a [$\pm$ 45/0] laminate of 1.5 mm thickness located on the external surfaces of the blade root were studied, but did not lead to much difference in the resultant σ_2 caused for the extreme thermal load.

Shear stress failure in the composite in planes 1-3 and 1-2 are governed by the shear strength of fibre, matrix or fiber-matrix bond. Whichever is the first limiting failure mode, shear stress in the 1-3 or 1-2 planes tend to generate a failure surface in the longitudinal direction of the fibres, creating an interlaminar failure. Figure 3.6b shows the shear stresses thought the same line AB. σ_{23} in the composite region is on the order of 2 MPa, below the shear strength of 7 MPa. σ_{12} has a maximum of 12 MPa near the grout interface, which is almost half of the strength obtained by Cormier.

Carrot with Thermal and Compressive Loads

The second FE case of the carrot connection analyzed simulated an ultimate load case under extreme cold temperatures. As stated in the IEC Standards, different conditions must be analyzed according to the chances of occurring simultaneously. There is no existing method to correlate extreme low temperatures with extreme wind conditions. This task is in fact part of the work being undertaken within the NSERC Wind Energy Strategic Network (WESNet). In the meantime, it was assumed that extreme cold temperatures and extreme wind speeds do not occur simultaneously.

Table 3.4: Tsai-Hill criterion in the composite region of a carrot section

2-dir [cm]	σ_1 [MPa]	σ_2 [MPa]	σ_{12} [MPa]	${\sigma_1}^2/{\sigma_1^T}^2$	$-\sigma_1\sigma_2/{\sigma_1^T}^2$	${\sigma_2}^2/{\sigma_2^T}^2$	${\sigma_{12}}^2/{\tau_{12}^F}^2$	Tsai-Hill criteria
0.36	-8.0	19.9	11.2	3.01E-04	7.48E-04	2.7	0.2	2.9
0.41	5.6	16.9	3.2	1.49E-04	-4.48E-04	2.0	1.65E-02	2.0
0.46	2.3	17.4	1.5	2.44E-05	-1.87E-04	2.1	3.70E-03	2.1
0.52	0.2	17.7	-0.3	1.69E-07	-1.58E-05	2.2	1.55E-04	2.2

Therefore, a reasonable indicator of the ultimate load case for extreme cold temperature conditions could be defined as a parked turbine subject to the one year extreme wind V_{e1}.

Figure 3.7 shows the stresses in the fibre-orientated coordinate system and σ_{vm} for the same line AB in the carrot section, but now under the compressive ultimate aerodynamic load produced in the carrot of a parked turbine under V_{e1} and subject to the -40°C typical extreme conditions stated in Table 3.1. Note that due to the bending loads, connections furthest away from the axis of bending experience both tensile and compressive loads; tensile loading is considered in the next section. The stresses in the composite section are similar to the stresses in the previous case depicted in Figure 3.6 (only thermal loads), indicating that for extreme cold conditions thermal stresses are more critical than the aerodynamic loads for the composite at the very base of the blade. Additionally, as expected, Fig. 3.7 shows that the steel takes most of the compressive stress. Again a high stress gradient is present in the interface of the grout with the carrot, in which σ_{vm} goes from 90 MPa to 25 MPa , below its strength of 57 MPa at -40°C (for a SF of 2.7).

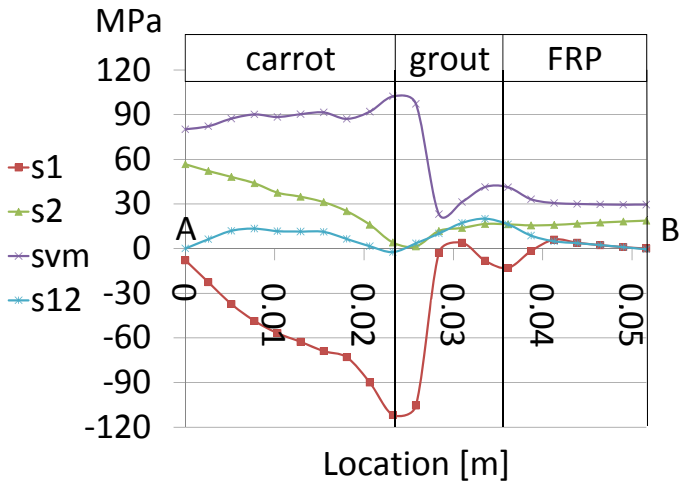

Figure 3.7: Ultimate compressive load of 144 KN plus a thermal load of 63 °C at the base of the carrot (path AB)

Carrot with Thermal and Tensile Loads

As demonstrated in the previous section, ultimate compressive loads do not substantially affect the performance of the already thermally loaded carrot near to the blade/hub connection. On the other hand, an ultimate tensile load case (i.e. the carrot opposite the maximum compressive loaded carrot of the previous section) generates stresses at the sharp end of the carrot where the thermal stress produces tensile forces in the fibre direction, since the carrot and the grout shrink more than the composite in the fibre direction. Therefore an ultimate tensile load case could compound such tensile stresses. Figure 3.8 shows the stresses trough the line CD at the sharp end of the carrot indicated in Fig. 3.4. It can be seen that σ_{vm} for the steel has a maximum of 170 MPa, well below its yield strength is 760 MPa (with a SF of 1.25). The σ_{vm} of the grout is also below its yield strength of 57 MPa, and it appears to be the most stressed zone at the end of the carrot, with a ratio σ_{vm}/σ_Y near 0.64. In the composite region , σ_1 is well below its strength of 259 MPa, and σ_2 is not significant with a value near 2 MPa. Thus, according to the stresses and Tsai-Hill criterion shown before, the end of the carrot exhibits good performance under thermal and ultimate tensile loads.

Experimental Static Carrot Tests

Wind turbine blade root studs were tested at NREL [10], including a room temperature static test of a specimen with a diameter similar to the carrot analyzed here, but of 20 cm length (versus 30 cm here). Failure was noted at 300 KN in the epoxy/FRP interface at the tip of the carrot and near the base. Note that this ultimate tensile failure occurs at 300 KN, well above the ultimate axial loads expected for a 1.5MW wind turbine (see Table 3.1). The failure mode is consistent with the stress concentration areas noted in the present work. Since exact geometry info was not available for the NREL test, the results were compared semi-quantitatively as described above.

3.6.2 T-bolt Connection

T-bolt Pretension and Room Temperature Operation

The second type of connection is the T-bolt, which was first analyzed under pure pretension. For the case of the embedded carrot connection, most of the preload

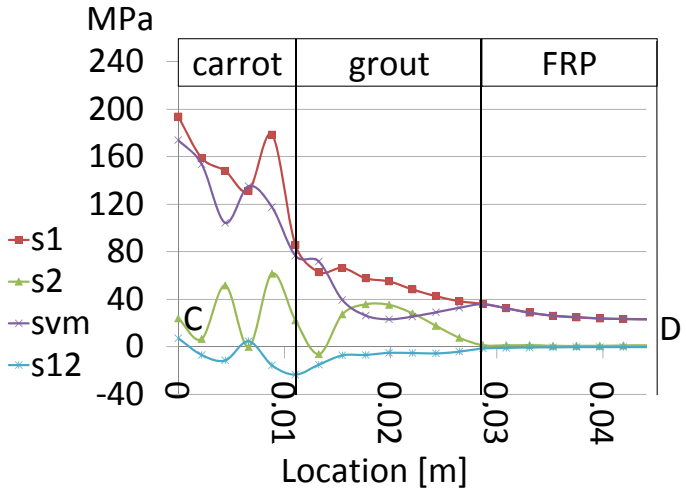

Figure 3.8: Ultimate tensile load of 144KN plus a thermal load of 63 °C at the end of the carrot (path CD)

tension is being taken directly by the bolt, the bearing ring and the carrot, all made of steel and causing almost no stress in the composite. This pretension prevents the blade root from separation, reduces the magnitude of the threaded bolt load cycles and does not cause close-to-failure areas due to the high strength of the steel. The pretension is present in the T-bolt design for all remaining cases studied. Unlike the embedded carrot connection, the pretension in the T-bolt connection stresses a large composite region between the cross bolt and the bearing ring. The pretension creates a compressive stress condition in the fibre direction, between 10 and 25 MPa in the pretensioned composite region.

Due to Poisson's ratio effects, the pure pretension case is also causing important stresses in the perpendicular-to-fibre directions, especially in the 2-direction where the compressive stress is around 5 MPa in the composite region. σ_3 is not significant for the T-bolt configuration since the free surface is reducing the stress in the out-of-plane direction. This also implies that the composite in a T-bolt connection has large strains in the 3-direction.

The interactive Tsai-Hill criterion predicts failure in a small region of the composite located between the bearing ring and the cross bolt. This failure condition under

pure pretension predicted by Tsai-Hill is generated fundamentally as a result of the high anisotropy of the composite strengths in the perpendicular to fibre direction. This illustrates the fact that this criterion fits better with moderately orthotropic material. All the other criteria including the decomposed Hashin criterion do not show failure for the pure pretension case.

T-bolt with Ultimate Loads

For the case of the pretensioned T-bolt subject to room temperature and under an ultimate compressive load generated by a V_{e1} gust, the compressive stress in the pretensioned composite region varies between 70 and 140 MPa, still well below the composite strength σ_1^C.

T-bolt with Thermal Loads

The second pretensioned T-bolt model analyzed here emulates an extreme cold condition of -40°. This thermal load increases the compressive stress acting in the fibre direction since the steel bolt shrinks more than the composite in that direction. The cross bolt transmits that extra compressive stress through the pretensioned composite region. Figure 3.9a shows the distribution of σ_1. There is a concentration of stress around the bolt/cross bolt joint region as high as 120 MPa. As was mentioned above, the pretension of the bolt produces a compressive stress in the matrix due to the perpendicular to fibre expansion of the pretensioned composite generated by the Poisson's ratio. The extreme thermal load reverses this condition by generating a tensile region especially in the 2-direction all throughout the composite. This 2-direction tensile stress is the result of the CTE mismatch between the composite and the steel of the pitch bearing in the 2-direction (the CTE of the composite in the perpendicular-to-fibre direction is twice that of steel). The steel bolt is attached to the bearing ring which is fully constrained on its bearing race face, and this configuration restrains the contraction of the composite in the 2-direction, in turn creating a high tensile stress region in the blade root. The σ_2 due to the thermal load is maximum in the pretensioned composite region and around the cross bolt. Figure 3.9b shows σ_2 in the section β indicated in Fig. 3.9a, where there is a massive failure region with σ_2 above 17 MPa. The interactive Tsai-Hill criterion detects this failure region, and

the maximum stress and Hashin matrix criteria indicate a matrix failure mechanism due to high transversal stress (σ_2).

T-bolt with Thermal and Compressive Loads

The third case analyzed is a T-bolt connection subject to an ultimate compressive load arising from an extreme one year gust V_{e1} and an extreme thermal load of -40°. This case increases the stress in the fibre direction, especially near the non-pretensioned composite region around the cross bolt. The cross bolt is uniformly transmitting this extra compressive stress to the pretensioned composite region and bolt. Regardless of this high compressive stress (which is near 90 MPa) the fibre-direction stress is far from fibre failure.

Interestingly, the compressive ultimate load caused by V_{e1} reduces the tensile stress in the perpendicular to fibre direction, most notably in the 2-direction. This reduction results from Poisson ratio and the high σ_1, expanding the composite in the transverse direction. Therefore, this ultimate compressive case in fact reduces the extent of matrix failure in the pretensioned composite region, which now concentrates near to the bearing ring and close the cross bolt. This reduction of σ_2 due to the ultimate compressive load is shown in Fig. 3.10 which depicts the stresses through a line PQ indicated in Fig. 3.9b. Since an ultimate tensile case reduces the compression in the 1 and 2-direction, the worst case for a T-bolt connection is the pure extreme thermal load.

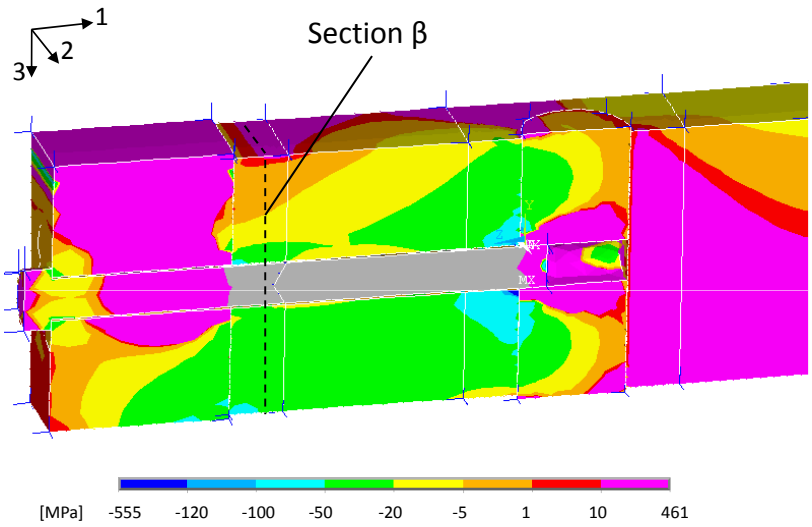

(a) Fiber-orientated stress (σ_1)

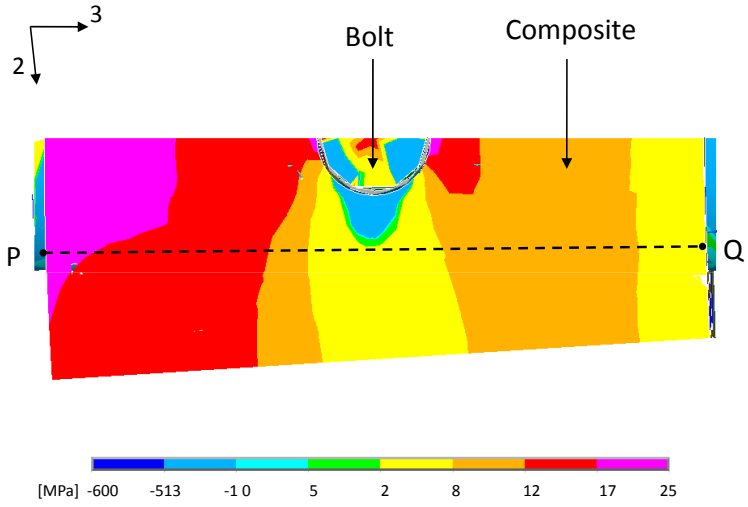

(b) In plane perpendicular-to-fibre stress (σ_2)

Figure 3.9: Stress in T-bolt blade connection subject to an extreme temperature of -40°C

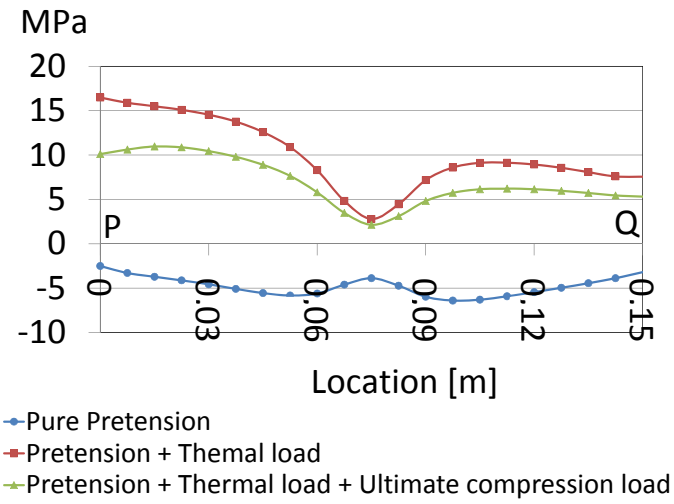

Figure 3.10: Perpendicular-to-fiber stress σ_2 in a T-bolt connection under different thermal and mechanical conditions

Chapter 4

Fatigue

For the case of static damage analysis, the maximum stresses are expected to occur in the root of the blade due to the large bending moments and structural details. On the other hand, fatigue performance depends on the number, amplitude and magnitude of the stress/strain cycles. Gravitational forces, in addition to flapwise and edgewise bending moments create complex load cycles acting on the blade. Fatigue estimation therefore requires an analysis of the entire blade.

This chapter analyzes the stress/strain fatigue cycles on the whole blade and determines areas and magnitude of the fatigue response at cold temperatures. Fatigue loads and fatigue composite properties were estimated. Later, the natural frequency variation was analyzed, together with stresses due to increased blade stiffness, root bending moment changes due to increased air density, and lifetime fatigue damage.

4.1 Blade Model

The static analyses presented in Chapter 3 studied the stresses generated by extreme wind conditions and temperatures. Fatigue analysis considers the cumulative damage of lifespan loads acting on the blade due to normal operational conditions.

The NREL code FAST (see Appendix A for details) was used to determine the operational loads seen by the the wind turbine blade. The FAST inputs used in this analysis included: active pitch control; all tower, blade and drivetrain mode DOFs activated; no yaw; and variable speed control activated. The wind inflows were obtained by TurbSim[39]. The fatigue load case was defined according to the 1999 IEC Standards (Second Edition) case 1.2 for a Class I turbine.

The structural blade model was built with the NREL code NuMAD. The details of the structural design are presented in Appendix C. The NuMAD model of the blade contains 19 stations. The airfoil sections [44, 45] were scaled to match the chord dimensiond and airfoil profiled described in the WindPACT Turbine Rotor Design Study [37].

The ANSYS FE model generated by NuMAD treats the blade at laminate and ply level using orthotropic shell elements in ANSYS. The blade was cantilevered at the root using the NuMAD option to do so, i.e. all nodes of the plane simulating the root/hub interface are constrained in all directions. Results from both linear (Shell99) and non-linear (Shell91) layered structural shell elements were compared, and no differences in the estimation of stress were found. Linear elements were therefore used throughout the remainder of the current study to save computational time. Figure 4.1 shows a section of the FE blade model in ANSYS. As for the static analyses, several mesh sizes where evaluated to check the convergence of the FE model. The results showed low variation in stress magnitude in the critical areas of the connection above 50,000 elements. The final FE model contains over 150,000 elements to ensure sufficient resolution results.

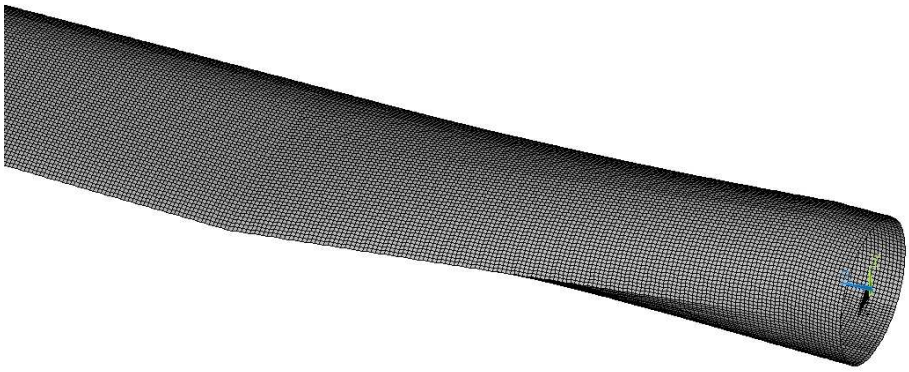

Figure 4.1: Section of the FE blade model

Aerodynamic and body forces acting on the blade root were obtained using FAST [38] by means of 600 s time-marching simulations. The resulting edgewise and flapwise bending moments were applied to the ANSYS model by means of distributed loads acting on the blade surfaces. These nodal loads mimic the different aerodynamic and body loads acting in each section of the blade. To determine the distributed loads, five 'gauges' were defined along the blade using FAST. The gauges were located at 0.25R, 0.5R, 0.75R, 0.95 and 1R. Each gauge defined in FAST stores the acceleration of the stations defined for the gauge locations in the flapwise and edgewise directions (according to the blade local axis). Figure 4.2 shows the acceleration at each blade gauge for room temperature conditions (air density of 1.225 kg/m^3) and a wind speed of 12 m/s. In the case of the flapwise direction, the gauge acceleration estimated is the average for 600 s of normal turbine operation. The edgewise accelerations show the acceleration seen by the blade stations in the horizontal position, when body forces and drag produces a maximum downward load.

Using these gauge accelerations and the distributed mass of the blade obtained from the FAST file *BaselineBlade.dat* (see Appendix B) the total load per unit span acting at each station can be estimated (load per unit span equalling mass per unit span times acceleration). Table 4.1 shows the loads acting on each blade station of a 1.5 MW wind turbine operating at 12 m/s wind speed.

Table 4.1: Dynamic response of blade stations for a 1.5MW wind turbine working at 12 m/s wind speed

	0.25R	0.5R	0.75R	0.95R	1R (33.25m)
Mass $[kg]$	3,017	1,250	627	122	20
Average flap acceleration $[m/s^2]$	0.4	3.2	9.5	13.2	14.6
Average flap load $[N/m]$	1,337	3,954	5,947	1,607	290
Downward edge acceleration $[m/s^2]$	0.19	0.48	0.60	0.79	0.82
Downward edge load $[N/m]$	640	480	414	110	20

Using these gauge loads, the nodal distributed loads acting on the blade skin were determined by assuming a smooth load distribution between the gauges. A generic nodal load distribution was then defined by scaling the loads by the total root bending moment on the blade and assuming uniform loads in the chordwise direction. In other words, the integrated bending (flap or edgewise) produced by all the distributed nodal loads acting on the FE blade model equals a given root bending moment. Then, the

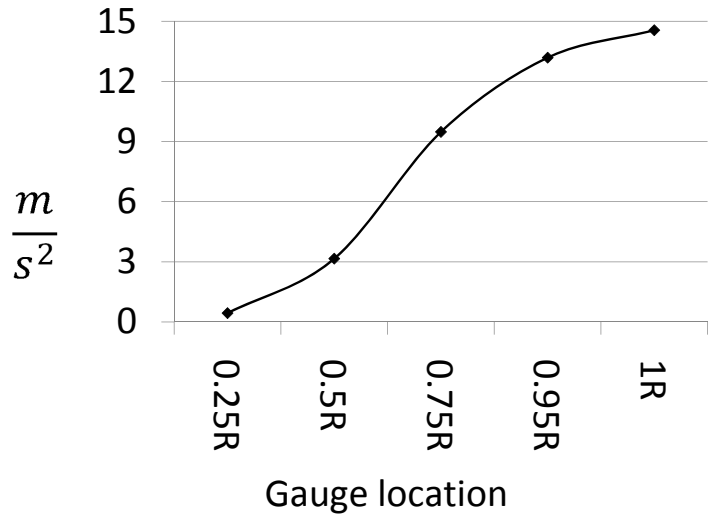

(a) Flapwise (average over 600 second)

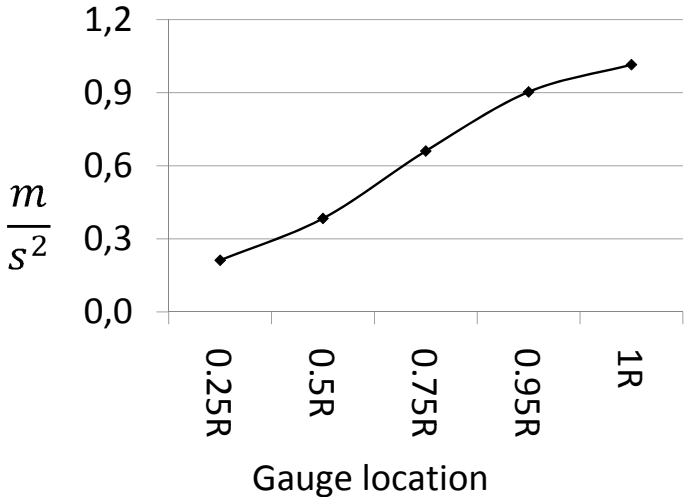

(b) Edgewise (maximum)

Figure 4.2: Acceleration at each blade gauge for room temperature (air density of 1.225 kg/m^3) and a wind speed of 12 m/s

resulting nodal loads were applied on the FE blade model to both upper and lower skin.

The distribution patterns of the gauge accelerations given in Table 4.1 (for 12 m/s and room temperature) were used to estimate all the distributed nodal loads at other wind speeds. It was found that nodal distributions at other wind speeds were quite similar to the 12 m/s case, and the analysis procedure was greatly simplified by simply scaling the generic distribution by the root bending moments experienced by the blade at other wind speeds. The load gauge patterns were therefore not changed to determine nodal loads at wind speeds different than 12 m/s.

For fatigue analysis, the overall procedure followed was:

1. Carry out time-marching simulation in FAST for each wind speed of interest.

2. Identify root bending moments (flap or edgewise) as relevant by means of spectrum analysis (rainflow counting) using Crunch.

3. Determine the peaks of the first cycle contributing to fatigue damage (maximum and minimum bending moments).

4. Apply the maximum bending moment of the cycle to the blade FE model in ANSYS using nodal distributed loads based on the generic loading distribution as described before. Store the resulting stresses occurring at each node.

5. Apply the minimum bending moment of the cycle to the blade FE model. Store the resulting stresses occurring at each node.

6. Carry out the fatigue computations described in §4.3 at each node using custom ANSYS macros and stored stress data.

7. Continue analysis with the next cycle contributing to fatigue damage.

In addition to the edge and flap nodal loads described above, a uniformly distributed axial load was also included in the model to represent centripetal forces caused by the rotating blades. In the estimation of fatigue damage, this distributed nodal axial load matches the total axial load acting at the root of the blade and is a function of the turbine rotational speed.

It should be noted that the loads obtained from the WP1.5MW machine simulated in FAST were applied to the detailed blade model described in this section.

Although the structural properties of the WP1.5MW machine's blades are similar to the baseline detailed structural model, they are not identical. A refinement of the current study could repeat the analyses presented here using as inputs to FAST blade definitions taken from an analysis of the baseline blade's structural properties. For the current analysis however, the loads are representative and considered to be valid for determining the criticality of fatigue loading at cold temperatures to MW-scale blades.

4.2 Material Fatigue Properties

Fatigue property information for composites at cold temperatures is even more sparse that the static properties discussed in §3.4. Griffin [41] describes the properties for the blade shell of a standard 1.5 MW turbine in the WindPACT Turbine Design Scaling Study, at room temperature. The details of the shell layup is given in Appendix C. The skins and spar cap are E-glass/epoxy laminates. The blade layers include a triaxial fabric named CDB340 with 25%, 25%, and 50% distribution of ±45°, and 0°fibres respectively. In that work, the spar cap laminate itself is made of alternating layers of triaxial and uniaxial fabric, with 70% uniaxial and 30% off-axis fibres by weight.

The current study adopted the same composite layup schedules, with estimates of the material properties made from the available data in the literature and the author's collaborating researchers' available experimental data.[1] The fibre volume of the layers is 40% in those experiments. Table 4.2 shows the derived base properties for blade layers at room temperature and -40°C.

Fatigue failure analysis in this work considers just the 0°orientation stress, which is orientated with the longitudinal blade axis and referred here as coordinate z. This simplification is based on the fact that y and x stresses are one order of magnitude lower than σ_z. The stiffness properties in all three dimensions obviously contribute the stresses in the z direction.

Several approximations were made to estimate composite properties at cold temperatures. First, the variation of E_1 and E_2 of the UD composite material described in Table 3.2 (with a V_f=55%) was used again here. E_1 increased by 3% and E_2 by 30%. Secondly, the same variation was applied to define E_1 and E_2 at cold tempera-

[1]This is ongoing experimental work that has to date only included uniaxial composite specimens.

Table 4.2: Composite layer properties of 1.5 MW wind turbine blade

23 °C/ Dry composite					
	Gel coat	Random mat	Triaxial fabric	Balsa	Spar cap
E_z [MPa]	3.4	9.65	24.2	2.07	27.1
E_x [MPa]	3.4	9.65	8.97	2.07	8.4
ν_{zx}	0.3	0.3	0.39	0.22	0.37
G_{zx} [MPa]	1.38	3.86	4.97	0.14	4.7
ρ $[kg/m^3]$	1.23	1.67	1.7	0.14	1.7
-40°C/ Saturated composite					
E_z [MPa]	4.4	10.71	26.9	2.07	30.15
E_x [MPa]	4.4	10.71	9.98	2.07	9.29
ν_{zx}	0.4	0.3	0.3	0.22	0.37
G_{zx} [MPa]	1.77	4.91	6.33	0.14	5.97
ρ $[kg/m^3]$	1.23	1.67	1.7	0.14	1.7

tures for the unidirectional material A260 described in Griffin [41] (with a V_f=40%). Then, the properties of this unidirectional composite material at cold temperature was used to estimate the Young's modulus of the spar cap layer at cold temperatures by Classical Laminate Theory (CLT) as described in Eq. (4.1) [11]. The material was defined as a combination of three symmetric cross-ply unidirectional layers of A260 with 70% (by weight) of 0°, 15% of −45°, and 15% of +45°fibres. This modelling results an E_z of 30.15 MPa for the spar cap at cold temperatures, 11% higher than room temperature as can be seen in Table 4.2. Finally, this percentage change in E_z of 11% of the spar cap layer is used to increase E_x. E_z and E_x of the triaxial fabric and random mat layer were also increased by the same factor of 11%.

$$
\begin{aligned}
& E_z = (A_{11}\, A_{22} - A_{12}^2)/A_{22} \\
& where \;\; A_{ij} = 0.7\, Q_{ij}^{A260[0^\circ]} + 0.15\, Q_{ij}^{A260[+45^\circ]} + 0.15\, Q_{ij}^{A260[-45^\circ]} \\
& \qquad Q_{11} = E_z/(1 - \nu_{zx}\, \nu_{xz}) \\
& \qquad Q_{12} = \nu_{zx}\, E_x/(1 - \nu_{zx}\, \nu_{xz}) \\
& \qquad Q_{22} = E_x/(1 - \nu_{zx}\, \nu_{xz})
\end{aligned} \tag{4.1}
$$

The same procedure described above was done for the shear modulus at cold temperature. Therefore, for the spar cap layer, the G_{zx} factor representing the difference between room and cold temperature was found 27%. The same factor was then used to increase G_{zy} and the shear modulus of triaxial fabric and random mat layer.

The Poisson's ratios of the skin materials were not modified at cold temperatures. The gel coat (epoxy) Young's modulus was obtained from Choi [13]. Finally, the shear web was assumed to have similar properties the triaxial layer.

4.3 Fatigue Failure Criteria

Fatigue analysis of composites is difficult due to the composition and complex characteristics of the fibre-matrix interactions. Unlike ultimate stress composite analysis in which there is at least some agreement, fatigue criteria are still an ongoing and active subject.

Deggrieck and Van Paepegem [22] classify fatigue models for wind turbine applications into fatigue life models based on S-N curves, and residual strength (or residual stiffness) models. Unlike isotropic materials, stresses in composite materials vary dramatically within the different structures and layers, and more importantly, a composite's stiffness changes with ageing.

Log-log and lin-log models are the main models used for composite fatigue failure prediction in wind turbine blades. S-N formulations are functions of the stress range (amplitude) and mean stress, which can both be specified by maximum stress and the stress ratio $R = \frac{\sigma_{max}}{\sigma_{min}}$. In general, each S-N curve must be obtained experimentally for different stacking sequences, different ply orientations, different R values, and for the relevant stress/strain directions in the composite (e.g. longitudinal and transverse directions). A distinctive characteristic of composite materials is that unlike ferrous steel and titanium, the S-N curves are characterized by the absence of a fatigue limit. Therefore, every cycle must be considered to cause damage. Mandell and Samborsky [8] state that composites with well aligned fibres or multi-directional reinforcement tend to follow an exponential model (i.e. a linear relationship on a semi-log plot), whereas woven fabrics and chopped strand, which are not common in the wind turbine industry, tend to behave non-linearly on a semi-log plot. The Germanischer Lloyd (GL) wind standard recommends a log-log curve for polyester and epoxy matrix for constant R ratios.

To obtain equivalent stresses, the simplest and most commonly used Constant Life Diagram (CLD) is the linear Goodman diagram in which the strain/stress amplitude decrease linearly with increasing mean strain for a given fatigue life, with zero at a mean strain equivalent to the ultimate compressive or tensile strengths. The GL standard recommends a modified version of the linear Goodman diagram in which the peak is moved toward the right (positive mean stresses) in order to reflect the asymmetry of the CLD seen in experimental data. The compressive and tensile fatigue strength performances of composites are governed by different mechanisms and this fact is therefore mirrored in the CLD. Under tension, the composite is governed by the fibre, whereas in compression matrix and matrix-fibre interactions predominate.

To account for cumulative fatigue damage, Burton [24] states that in wind turbine design it is a common practise to use the rainflow counting algorithm and Miner's rule. However, other researchers have noted significant differences between fatigue life predictions and reality using this approach. One of the reasons is that Miner's rule and the rainflow counting algorithm do not consider the sequence of the loads that affect blade sections, i.e. they do not consider the stress-strain temporal history. Composite coupons seem to behave differently depending on whether they are subject to a load spectrum that mirrors actual operational conditions in which the loads are variable over time, compared to cases in which they are subject to an equivalent series of constant R value loads with variable magnitude. Burton, quoting van Delft, stated that such differences in lifetime prediction for specimens under variable spectrum loads were up to 100 times less than the lifetime predicted using constant amplitude, reverse loading and Miner's rule.

It is interesting that most of the fatigue criteria are based on simple non-interactive methods, unlike the numerous interactive models for static composite failure discussed in §3.5. Sutherland [46] found good agreement between linear and bi-linear Goodman diagrams. He also stated that linear and bi-linear models are more conservative than the composite data estimated by Mandell and Samborsky [8], specially for compressive stresses near the transition to tension.

Based on the points elucidated in the previous discussion, and in the absence of more accurate models, the current work presented here utilizes a linear Goodman diagrams for equivalent stresses. Also, it uses a lin-log approximation for the S-N

curves as described by Mandell and Samborsky [8], and shown in Eq. (4.2)

$$s/s_0 = 1 - b log N \tag{4.2}$$

where N is the number of cycles to failure and s_0 is the cycle strength used to normalize the curve.

At room temperature, fatigue coefficients for tensile stress cycles (R=0.1) were defined based on Mandell and Samborsky [8]. The parameter b ($R = 0.1$) for the spar cap mixture layer was defined as 0.100. It was assumed to have a fatigue behaviour similar to the composite materials labelled as DD5E and DD5P $[0/\pm 45/0]_s$ in that study. For the triaxial fabric (CDB340) b was defined as 0.115, similar to materials with 50% of the fibres in the 0°orientation.

As mentioned previously, collaborating specialists at ETS are currently preforming a fatigue campaign on unidirectional composites (V_f=57.5%) under cold temperature (-40°), moisture and thermal cycling. Normalized results[2] show that tensile fatigue cycles ($R = 0.1$) at cold temperatures slightly reduce the fatigue strength in dry composites. On the other hand, at -40°C water saturated (0.5% by weight) composite samples slightly increase their fatigue performance. That increase in the fatigue performance of saturated composites at -40°C decreases the tensile fatigue coefficient b ($R = 0.1$) by around 5% (the lower the value of b, the higher the fatigue strength).

The estimation of b ($R = 0.1$) for cold temperatures in the spar cap and triaxial layers was obtained by modifying b in the same proportion to the experimental fatigue strengths. Therefore, between 23°C and -40°C b is reduced by 5%. For temperatures between room temperature and -40°C the values of the engineering properties and b were linearly interpolated. Table 4.3 shows the estimation of b at 6.8°C and -14°C corresponding to the six warmest and coldest months in the northern Canadian locations indicated in §2.1.

Is important to notice that fatigue strength is extremely sensitive to b, especially for low stresses and materials with high fatigue strength (low b) due to the logarithmic relationship of fatigue behaviour. Consequently, for high cycle fatigue (low stress) the difference in accumulated damage is substantial for small variations of b. For example, a difference of 10% in the fatigue coefficient b leads to a difference of nearly 3 times in the number of cycles to failure. Finally, the load safety factor for bending moments

[2]These fatigue results were normalized relative to room temperature static strengths.

Table 4.3: Fatigue coefficients (b) of saturated composite for R=0.1 at cold temperature

	Triaxial fabric	Spar cap
23°C	0.115	0.100
6.8°C	0.114	0.099
-14°C	0.110	0.096

were defined as 1.00 according to the IEC Standard, and the material safety factor was defined as 1.93.[24]

4.4 Results

This section describes the results of the full-blade fatigue analysis. Recall from §4.1 that the applied root moments referred to in this section were actually applied as distributed loads according to a predefined nodal distribution.

4.4.1 Natural Frequency Variation

In dynamic cycling, large oscillations can occur in a system even due to small forces at some frequencies, particularly when these frequencies are close to the natural frequencies of the structure. The operation of a wind turbine generates a significant oscillating load due to the rotation of the blades which reach 20 RPM (0.33 Hz) for above-rated wind speeds of the 1.5 MW turbine analyzed here. This section studies the effect of cold temperature on blade natural frequencies to ascertain if any resonant conditions may be created by the stiffening of the structure at cold temperatures.

As expected, a variation in temperature increased the blade stiffness, thus modifying the natural frequencies of the blade. Table 4.4 shows the first four modal frequencies of the blade obtained from ANSYS. The increase in stiffness of the blade at -40°C augments the natural frequencies by around 5% (compared to 11% for the spanwise material stiffness). The mode shapes were only compared qualitatively and not found to vary significantly for cold temperatures.

Table 4.4: Natural frequencies of a 1.5MW turbine blade at cold temperature [Hz]

	23°C	-40°C
First flapwise bending	0.53	0.55
First edgewise bending	0.64	0.67
Second flapwise bending	1.59	1.68
Second edgewise bending	2.67	2.77

The FAST code includes vibration (with and without damping) by means of a user-defined polynomial shape modes (edge and flapwise). Also, FAST computes its own

natural frequencies for the modes, based on input sectional stiffnesses. As mentioned in §4.1 this work did not modify the FAST input mode shapes at cold temperatures since little variation was found in natural frequencies. It is also important to notice that [41] states a broad range of values for spar cap thickness, going from zero to 10%. Spar cap thickness used in this work was defined as 5% of local maximum section thickness (see Appendix C). Since spar cap thickness affects blade stiffness, future work must consider the effect of natural frequencies for different spar cap configurations. According to the results, it seems that blade first natural frequencies found in this work are somewhat lower than those in the FAST model.

4.4.2 Stresses Due to Increased Blade Stiffness

Cold temperatures were found to increase the blade stiffness, which changed the stresses in the blade structure. To analyze this effect, the FE blade model was subject to a 550 kNm edgewise bending moment. This load represents a very distinctive cycle of 900 KNm range (peak-to peak) and 100 KNm mean in the 1.5 MW wind turbine working between V_r and $V_{cut-out}$. The highly stressed regions of the blade under this load are the leading and trailing edges near 0.15 R, i.e. the tapered region between the root and the first airfoil section located at 0.25 R. Table 4.5 shows the average 0°stress of the tensile region for every layer.

Table 4.5: Change in maximum stress due to increased stiffness at cold temperatures

	Blade skin layer				
	Gel coat	Random mat	Triaxial	Balsa	Triaxial
Thickness [mm]	0.51	0.38	0.89	10 (aprox.)	0.89
σ_z at 23°C [MPa]	8.5	21.3	22.3	5.2	22.9
σ_z at -40°C [MPa]	10.5	21.7	22.6	4.6	23.3
Stress difference	23%	1%	2%	-10%	2%

A temperature of -40°C raises the 0°stress nearly 2% in the composite layers. On the other hand, for high cycle fatigue (low stress), fatigue damage is relatively insensitive to the magnitude of the stress. As an example, for stresses below 5% of the Ultimate Tensile Strength (UTS), doubling the stress in the triaxial layer boosts fatigue damage by only around 20%. Therefore, a stress increment of 2% due to a change in the blade stiffness is negligible to the lifespan fatigue damage.

Additionally, off-axis stresses and shear stresses are one order of magnitude lower than the 0°orientation stresses. Also, notice that the gel coat stress is much lower than stress in the structural triaxial layer. Note that these estimates do not include internal thermal stresses (i.e. no CTE were considered); these effects would be complex to include and require very detailed modelling or an experimental campaign on the candidate composite layups.

4.4.3 Root Bending Moment Changes Due to Increased Air Density

Cold temperatures increase air density, significantly so at the extremes seen in Canada. At 23°C and one atmosphere, the (dry)[3] air density is 1.225 kg/m^3. At -40°C the air density is 1.5 kg/m^3, 22% higher. This affects the aerodynamic loads and subsequently affects induced blade bending moments. Figure 4.3 shows the lifespan root bending moments obtained from a full lifetime series of FAST simulations for air densities corresponding to 23°C and -40°C over the entire set of operational wind speeds. Cold temperatures raise the flapwise bending moments, adding nearly one million cycles with magnitudes above 1400 KNm (amplitude). These additional million cycles are relatively low in comparison with the total number of flapwise bending moments, causing little additional fatigue damage. On the other hand, lifespan edgewise bending moments are not dramatically affected by the change in air density. This is due to the pitch control regulating the power output at wind speeds above V_r.

4.4.4 Lifetime Fatigue Damage

The fatigue blade damage estimation developed here is based on FE analysis. One of the advantages of this methodology is its low cost in comparison with a full blade test. Also, specially for the type of loads generated in the operation of a wind turbine, an actual fatigue test can not properly simulate high cycle fatigue due to the time that is required to apply 10^8 low stress cycles. On the other hand, a full blade test is a more accurate approach in terms of structural interaction and material discontinuities, specially for materials as complex as composites.

[3]The humidity level has only a small effect on air density.

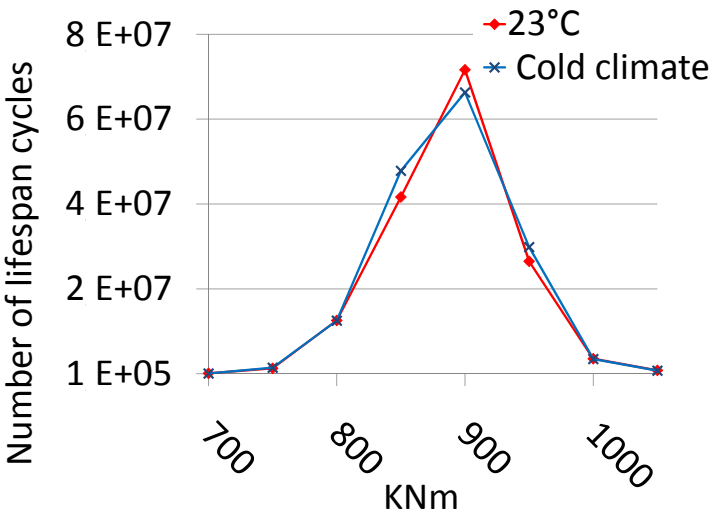

(a) Edgewise bending moments

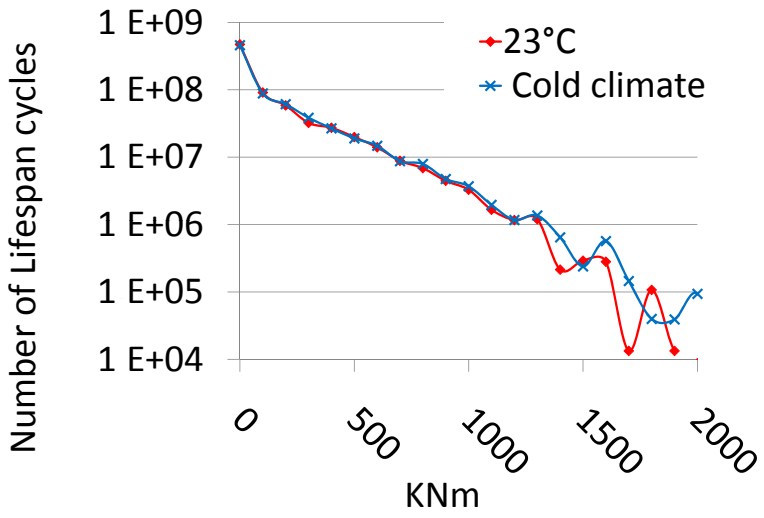

(b) Flapwise bending moments

Figure 4.3: Change in root bending moments (amplitude) in a 1.5MW turbine due to increased air density at cold temperatures

The bending moments used to load the blade for the full lifetime fatigue damage evaluation were obtained from FAST at 2 m/s increments within the range $V_{cut-in} \leq V \leq V_{out}$ for three air densities:

1. 1.225 kg/m^3, representing 23°C
2. 1.296 kg/m^3, representing 6.8°C (average temperature for the 6 warmest months)
3. 1.387 kg/m^3 for -14°C (the average temperature for the 6 coldest months)

Fatigue load spectra were extracted from 600 s simulations using the NREL code Crunch which employs a rainflow counting algorithm. Flapwise bending moments were binned every 100 KNm. Edgewise bending moments were binned every 50 KNm. The total number of lifespan cycles acting on the blade was then obtained from a Weibull wind distribution with an average wind speed of 10 m/s (hub-height) according to the IEC Standards. The blade mode shapes in FAST were kept constant for all temperatures based on the model analysis of section 4.4.1. The materials in the ANSYS FE model was defined according to Table 4.2.

The blade was cantilevered at the root and the edge or flapwise bending moments were applied individually in ANSYS as distributed loads on the skin blade nodes to represent aerodynamic and body forces, as described in §4.1. On the same note, centrifugal nodal loads were applied for each wind speed case representing the rotational speed in normal operational conditions. Finally, mean bending moments were found to be small and were neglected and considered as zero for the determination of fatigue damage in this work.

Table 4.6 shows the lifespan fatigue damage (20 years) for the blade subject to different hygrothermal conditions. The damage was computed in the flapwise region near 0.15R, i.e. the tapered region between the root and the first airfoil section located at 0.25R. The results represent the worst nodal locations in that region.

At dry conditions and room temperature, the triaxial layer undergoes a damage of approximately 47% due to edgewise bending moments. Most of that damage is caused by a high number of high magnitude cycles.

The damage in the spar cap region is one order of magnitude smaller in comparison with the damage in the triaxial layer. This difference is caused due to the 70% content of 0°direction fibres in the spar cap mixture versus 50% in the triaxial layer (by weight).

Table 4.6: Lifespan (20 yrs) fatigue damage of a 1.5 MW wind turbine blade

	23 °C/Dry composite	
	Triaxial fabric	Spar cap
Edgewise	31%	1.6%
Flapwise	16%	0.8%
Total damage	47%	2.3%
	North Canada /Saturated composite	
Edgewise	19%	0.9%
Flapwise	9%	0.4%
Total damage	28%	1.3%

At cold temperatures and saturated conditions, the triaxial fabric experiences a damage of 28%, nearly half of the damage at room temperature. This improvement in fatigue performance is due primarily to the variation in b (R=0.1) from 0.115 at room temperature to 0.114 and 0.111 at 6.8°C and -14°C respectively. As an example, a decrement of 3% in b brings about a 50% more damage for high fatigue cycles (low stresses).As was mentioned before, the increase in the magnitude of flapwise bending moments at cold temperatures and the increase of the blade stresses due to higher stiffnesses does not significantly affect lifespan fatigue damage.

Comparison of the damage between the compressive and tensile regions of the blade (flapwise loads) do not show significant differences. This is mostly due to the simplification used in this work of considering just the amplitude of the load cycles and not the mean. On the other hand, since fatigue damage for low stress is not very sensitive to stress magnitude, this assumption seems reasonable.

The results so far are not conclusive about the effect of hygrothermal conditions on fatigue strength. Improved material data as input to the numerical models, specifically experimental data at cold temperatures and high fatigue cycles, is required to verify these simulation results, now that the critical parameters have been identified in the current work. Likewise, the relatively small damage numbers in Table 4.6, especially for the spar cap, indicate that the nominal blade used was non-optimal even for room-temperature conditions. Further work could therefore repeat the current study with a more optimized design working closer to the limits of the safety factors.

Chapter 5

Conclusions

This work has examined the extreme cold conditions that characterize Canadian weather as they relate to wind turbine operation, especially in the far North regions. Such temperatures were determined to be in the range of -30°C for annual average winter temperatures, with 50 year return temperatures around -50°.

A reference 1.5 MW turbine model was used throughout this work, representative of a machine size suitable for installation in these more remote locations. It was determined that direct fully reversed gravitational and steady centrifugal axial forces account for just a small part of the load applied on the root connections of a wind turbine blade. Most of the connection loads are caused by the bending moments carried through the root to the pitch bearing. In the case of wind speeds below cut-out velocity, the pitch control of the turbine keeps the ultimate loads acting on the connections in the same order of magnitude for different air densities (i.e. different temperatures). For winds above cut-out, the ultimate loads acting on the connections of the blade are almost linearly proportional to the change in the air density for the case of a parked turbine.

At extreme cold temperatures of -40°C the total individual static connection loads are near 251 KN for the 1.5 MW machine studied. On the other hand, the results have shown that regardless of the increment in the loads due to the increase in the air density, thermal stresses are more relevant, and are in some parts of the blade root, critical. Moreover, while there is a significant change in the strengths in the fibre direction of the composite at cold temperatures (in fact increasing the strength), the main critical effect of the extreme cold temperature are the strains due to the mismatch of the CTE of blade root constituents and the orthotropic CTE of the

composite in the transverse direction.

For the case of a embedded carrot connection, the results have shown that thermal loads produce stresses in the interface of the grout along the carrot. The critical areas are the end of the carrot and the area close to the hub/blade connection. The FE models developed here have shown that the sharp end of the carrot is affected by the large mismatch between the low CTE of the composite in the fibre direction and the relatively high CTE of the grout and the steel. At low temperatures, the carrot shrinks more than the composite in the fibre direction creating a high strain condition. The stress produced in this zone is a tensile stress that mainly affects the grout interface. However, it seems that this fibre orientated tensile stress is well below failure, even for the case when the turbine is subject to a extreme temperature of -40°C and a wind speed of 52 m/s (V_{e1}).

Under an extreme thermal loads, the section of the carrot close to the hub connection plane shows a high transverse-to-fibre stress. The base of the carrot is strongly influenced by the high shrinkage deformation of the composite in the 2-direction creating a tensile σ_2. The strength in this direction is matrix governed and has a low tensile strength that warrants further experimental characterization.

For the case of the T-bolt connection, the increase in the strength of the composite at cold temperatures helps to support the pretension and ultimate compressive load in the fibre direction. The pretension of the cross bolt significantly contributes to the fibre orientated stress creating compressive stress near 20 MPa in the composite region between the cross bolt and the hub ring. Due to the high performance of the composite in that direction, the pretension does not significantly contribute to static failure.

As was the case for the carrot system, an extreme thermal load is creating a high transverse stress σ_2 due to the mismatch of CTE and constraints of the system. Therefore, thermal loads in the composite near the pitch bearing were shown to be of concern in both kinds of connections.

Furthermore, the high σ_2 created by the extreme thermal load varies with the thickness of the blade root. In simulations with thicker shells, it was found that adding additional material opposes the contraction of the composite in the 2-direction leading to higher stresses. The thickness therefore plays a key role in terms of the fibre direction stress and high transverse thermal stress.

Addition of off-axis materials to the root section models using layered solid elements did not greatly influence the results obtained. This could be revisited, particularly as experimental test data for layered coupons become available in the ongoing experimental test campaign.

It was found that a change in temperature from 23°to -40°increases blade stiffness around 11% in the 0°direction for a reference 1.5 MW wind turbine blade. Data from collaborating specialists at ETS suggests an improvement in fatigue performance for saturated unidirectional composites at cold temperatures.

Blade natural frequencies are not considerably affected by the increase in blade stiffness at cold temperatures. The difference between natural frequencies at 23°and -40°is less than 5% for first and second flap and edgewise bending modes. On the other hand, the change in stiffness slightly increases blade stresses. However, this rise in the stresses does not considerably affect lifespan fatigue damage.

The increase in air density at the cold temperatures typically seen in Canada adds nearly one million flapwise bending moment cycles. These additional flapwise loads do not severely affect lifespan damage, since the number of cycles is considerably lower in comparison to the total number of flapwise cycles during the lifespan of the blade. Edgewise bending moments are nearly constant at different air density conditions due to the effects of pitch control.

Overall, lifetime fatigue damage in the blade is reduced due to the improvement of fatigue strength at cold temperature in saturated composites. Fatigue damage of a blade operating in the Canadian northern climate is nearly half of the predicted damage at room temperature. The primary reason for this enhancement is the variation in the fatigue coefficient b.

5.1 Future Work

The static analysis has shown the critical role of the perpendicular to fibre strengths under tension σ_2^T at cold temperatures for blade root connections. In this work, σ_2^T at cold temperature was assumed 10% higher that at room temperature. Due to its importance in the performance of wind turbines working in Canadian cold weather, this estimate must be validated in future experimental work.

For the case of fatigue analysis, the results so far are not conclusive about the effect of hygrothermal conditions on fatigue strength. Experimental data at cold

temperatures and high fatigue cycles is required to verify the results obtained in this work including more research on non-unidirectional composite behaviour at cold temperatures. It is also critical to obtain a better understanding of fatigue damage for high cycle fatigue (low stresses).

Fatigue analysis in this work considered just 0°orientation stress, which are orientated along the longitudinal blade axis and referred to here as z oriented stresses. More work is necessary to better understand off-axis performance.

Other critical areas of interest are the shell-shell and shell-web bond lines. Small scale finite element models of these joints could provide a good understanding of the effect of cold temperatures at these potentially important sites where neat resin and reinforced composites layups may experience thermally induced stresses.

Finally, icing loads should be taken into account as well in future work. Icing certainly imparts modified aerodynamic loadings to the blades due by altering the section profiles, and this will undoubtedly affect the predicted structural performance of the blades.

Bibliography

[1] CanWEA, "Strategic wind power development plan: Wind vision 2025," tech. rep., www.canwea.ca/windvision_e.php, may 2009. 1

[2] X. Wang, G. F. Naterer, and E. Bibeau, "Experimental study of 3d blades and wind turbines under icing conditions," in *The Second International Green Energy Conference*, (Oshawa, ON), 2006. 1, 4

[3] J. Maissan, "Wind power development in sub-arctic conditions with severe rime icing," *Northern Review*, June 2001. 1, 4

[4] T. Laakso, H. Holttinen, G. Ronsten, L. Tallhaug, R. Horbaty, I. Baring-Gould, A. Lacroix, E. Peltola, and B. Tammelin, "State-of-the-art of wind energy in cold climate," tech. rep., IEA Wind Annex XIX, 2003. 1, 4, 12

[5] L. Cormier and S. Joncas, "Effects of cold temperature and freeze-thaw cycles on the mechanical properties of unidirectional glass fiber/epoxy composites," in *51st AIAA/ASME/ASCE/AHS/ASC Structures, Structural Dynamics, and Materials Conference* (AIAA, ed.), AIAA, January 2010. 2, 3, 4, 27, 28

[6] P. K. Dutta and D. Hui, "Low-temperature and freeze-thaw durability of thick composites," *Composites: Part B 27B*, pp. pp. 371–379, 1996. 2, 4

[7] P. Bronsted, H. Lilholt, and A. Lystrup, "Composite materials for wind power turbine blades," *Annual Review of Material Research, 35th Edition*, pp. pp. 505–538, 2005. 2

[8] J. Mandell and D. Samborsky, "Doe/msu composite material fatigue database: Test methods, materials and analysis," Technical Report SAND97-3002, Department of Chemical Engineering, Montana State University, December 1997. 4, 5, 27, 28, 54, 55, 56

[9] J. Rivera and V. Karbhari, "Cold-temperature and simultaneous aqueous enviroment degradation of carbon/vinylester composites," *Elsevier Composites*, pp. 17–24, 2001. 4

[10] S. Hughes, W. Musial, S. Ramey, M. Meadors, M. Jenks, R. Hunsberger, and D. DeShay, "Cold climate testing of double-ended fiberglass/stell root stud substructures for wind turbine blades," tech. rep., National Renewable Energy Laboratory, National Wind Technology Center, NWTC-ST-NPS/BMI-LF-02-0301-FR, 2001. 5, 41

[11] M. W. Hyer, *Stress Analysis of Fiber-Reinforced Composite Materials*. WCB McGraw-Hill, 1998. 5, 29, 30, 31, 53

[12] A. K. Kaw, *Mechanics of Composite Materials*. CRC Press, 1997. 5, 30

[13] S. Choi and B. V. Sankar, "Micromechanical analysis of composite laminates at cryogenic temperatures," *Journal of Composite Materials*, vol. 40, pp. 1077–1091, September 2005. 5, 27, 29, 54

[14] S. Usami, H. Ejima, T. Suzuki, and K. Asano, "Cryogenic small-flaw strength and creep deformation of epoxy resins," *Cryogenics*, vol. 39, pp. 729–738, June 1999. 5, 29

[15] F. Paris, "A study of failure criteria of fibrous composite materials," Report NASA/CR-2001-210661, George Washington University, Joint Institute for the Advancement of Flight Sciences, March 2001. 5

[16] C. Sun, B. Quinn, J. Tao, D. Oplinger, and W. J. Hughes, "Comparative evaluation of failure analysis methods for composite laminates," Report DOT/FAA/AR-95/109, U.S. Department of Transportation, Federal Aviation Administration, 1996. 5, 32, 33

[17] DNV, *Design and Manufacture of Wind Turbines Blades, Offshore and Onshore Wind Turbines*, October 2006. 5, 32

[18] D. Azzi and S. W. Tsai, "Anisotropic strength of composites," *Experimental Mechanics*, pp. 283–288, 1965. 5, 32

[19] S. W. Tsai and E. M. Wu, "A general theory of strength for anisotropic materials," *Journal of Composite Materials*, vol. 5, pp. 58–80, 1971. 5

[20] R. M. Christensen, *Mechanics of Composite Minerals*. Dover Publications, 2005. 5, 32

[21] Z. Hashin and A. Rotem, "A fatigue failure criterion for fiber reinforced materials," *Journal of Composite Materials*, vol. 7, pp. 448–464, October 1973. 5

[22] J. Degrieck and W. V. Paepegem, "Fatigue damage modelling of fibre-reinforced composite materials: Review," *Applied Mechanics Reviews*, vol. 4, pp. 279–300, 2001. 5, 54

[23] J. F. Mandall, D. D. Samborsky, and D. S. Cairns, "Fatigue of composite materials and substructures for wind turbine blades," Technical report SAND2002-0771, Sandia National Laboratories, March 2002. 5

[24] T. Burton, D. Sharpe, N. Jenkins, and E. Bossanyi, *Wind Energy Handbook*. 2001. 5, 17, 55, 58

[25] H. J. Sutherland and J. F. Mandell, "Optimized constant-life diagram for the analysis of fiberglass composites used in wind turbine blades," *Journal of Solar Energy Engineering*, vol. 127, no. DOI: 10.1115/1.2047589, pp. 563–569, 2010. 5

[26] A. Szekrenyes and J. Uj, "Finite element modelling of the damage and failure in fiber reiforced composites," *Research Group for Dynamics of Machines and Vehicles Hungarian Academy of Sciences*, 2002. 6

[27] C. Kong, J. Bang, and Y. Sugiyama, "Structural investigation of composite wind turbine blade considering various load cases and fatigue life," *Elsever*, pp. 2101–2114, 2004. 6

[28] L. R. McKittrick, D. S. Cairns, and J. Mandell, "Analysis of a composite blade design for the aoc 15/50 wind turbine using a finite element model," tech. rep., Sandia National Laboratories, SAND2001-1441, 2001. 6

[29] J. A. Paquette and P. S. Veers, "Increased strength in wind turbine blades through innovative structural design," technical report, Sandia National Laboratories, Wind Energy Technology Department, 2008. 6

[30] J. Locke and U. Valencia, "Desing studies for twist-coupled wind turbine blades," Technical Report SAND2004-0522, Wichita State University, 2004. 6

[31] D. D. Samborsky, A. T. Sears, J. F. Mandell, and O. Kils, "Static and fatigue testing of thick adhesive joints for wind turbine blades," in *2009 Asme Wind Energy Symposium*, 2009. 6

[32] P. S. Veers, T. D. Ashwill, and H. J. Sutherland, "Trends in the design, manufacture and evaluation ofwind turbine blades," *Wind Energy*, vol. 6, pp. 245–259, 2003. 6

[33] J. Deng, M. Lee, and S. Moy, "Stress analysis of steel beams reinforced with a bonded cfrp plate," *Composite Structures*, vol. 65, pp. 205–215, December 2003. 7, 24

[34] "Global meteorological forcing dataset for land surface modeling," tech. rep., CISL Research Data Archive Home, http://dss.ucar.edu/datasets/ds314.0/, 2009. 9

[35] "Wind energy atlas," tech. rep., Environment Canada, http://www.windatlas.ca/en/index.php, 2008. 9

[36] "National climate data and information archive," tech. rep., Environment Canada, http://www.climate.weatheroffice.gc.ca.html. 9

[37] D. Malcolm and A. Hansen, "Windpact turbine rotor design study," Mechanical report NREL/SR-500-32495, National Renewable Energy Laboratory, August 2002. viii, 14, 15, 48, 82, 83

[38] J. M. Jonkman and M. L. Buhl, "Fast users guide," Technical Report NREL/EL-500-38230, National Renewable Energy Laboratory, 2005. 14, 49, 75

[39] B. Jonkman and M. L. Buhl, "Turbsim user's guide for version 1.40," technical report, National Renewable Energy Laboratory, September 2008. 14, 47

[40] T. Ashwill, "Sweep-twist adaptive rotor blade: Final project report," Tech. Rep. SAND2009-8037, Sandia National Laboratories, 2010. 19

[41] D. A. Griffin, "Windpact turbine design scaling studies technical area 1-composite blades for 80- to 120-meter rotor," Technical report NREL/SR-500-29492, National Renewable Energy Laboratory, April 2001. vii, 21, 52, 53, 59, 83, 84

[42] Y. Yu and I. Ashcroft, "An experimental investigation of residual stresses in an epoxysteel laminate," *International Journal of Adhesion & Adhesives*, vol. 26, pp. 511–519, July 2005. 27

[43] T. Laakso, "Wind energy projects in cold climates," in *Committee of the International Energy Agency Programme for Research and Development on Wind Energy Conversion Systems* (T. R. C. of Finland, ed.), Technical Research Centre of Finland, 2005. 27

[44] D. Somers, "The s816, s817, and s818 airfoils," tech. rep., National Renewable Energy Laboratory NREL, NREL/SR-500-36333, 2004. 48

[45] D. Somers, "The s825 and s826 airfoils," tech. rep., National Renewable Energy Laboratory NREL, NREL/SR-500-36344, 2005. 48

[46] H. J. Sutherland and J. F. Mandell, "Effect of mean stress on the damage of wind turbine blades," No. DOI: 10.1115/1.1785160, ASME, October 2004. 55

[47] J. Petersen, "The aeroelastic code hawcmodel and comparisons," in *State of the Art of Aeroelastic Codes for Wind Turbine Calculations* (P. BM, ed.), vol. Annex XI, pp. 129–135, International Energy Agency/Technical University of Denmark, 1996. 74

[48] M. L. Buhl, "A comparison of wind turbine aeroelastic codes used for certification," Conference paper NREL/CP-500-39113, National Renewable Energy Laboratory, January 2006. 74

[49] J. Jonkman, "Modeling of the uae wind turbine for refinement of fast-ad," tech. rep., National Renewable Energy Laboratory, NREL/TP-500-34755, 2003. 75

[50] D. J. Laino and A. C. Hansen, "Aerodyn user's guide," tech. rep., Salt Lake City, December 2002. Prepared for the National Renewable Energy Laboratory under Subcontract No.TCX-9-29209-01. 76, 77

[51] R. Wilson, S. Walker, and P. Heh, "Fast-ad advanced dynamic code," Technical and users's manual OSU/NREL REPORT 99-01, Oregon State University, Department of Mechanical Engineering, 1999. 76

[52] J. Jonkman, "Dynamics modeling and loads analysis of an offshore floating wind turbine," Technical Report NREL/TP-500-41958, National Renewable Energy Laboratory, November 2007. 76

[53] P. J. Moriarty, "Aerodyn theory manual," Technical report NREL/EL-500-36881, National Renewable Energy Laboratory, December 2005. 77

Appendix A

NREL Codes

The National Renewable Energy Laboratory (NREL) in the US uses two codes for HAWT analysis, MSC.ADAMS[1] and NREL's Aeroelastic Design Code for Horizontal Axis Wind Turbines (FAST). The former is a multibody dynamics and motion analysis software used outside the wind industry as well. In fact, MSC, the software company that developed and commercializes ADAMS, claims that it is the most widely used software for dynamic analysis.

FAST is a public available code developed by the NWTC sponsored by NREL. The aerodynamic and inertial loads acting on the blade carrot in this work were determined by means of the code FAST, which is briefly described here. Figure A.1 shows a design process overview of ADAMS and FAST together with other NREL codes for wind design. Other aeroelastic codes used by the industry for 3-bladed HAWT are BLADED (distributed by Garrad Hassan and Partners Ltd), HAWC (developed by Riso National Laboratory, Denmark [47]) and BHawC (developed by Bonus Energy and Simens Wind Power). More information on aerolastic codes can be found from Buhl [48].

A.1 FAST

FAST is an aeroelastic code capable of estimating extreme and fatigue loads of two and three-bladed conventional HAWTs under given wind conditions. FAST includes two forms of operation. The first one is a time-marching mode in which wind tur-

[1] http://www.mscsoftware.com/Contents/Products/CAE-Tools/Adams.aspx

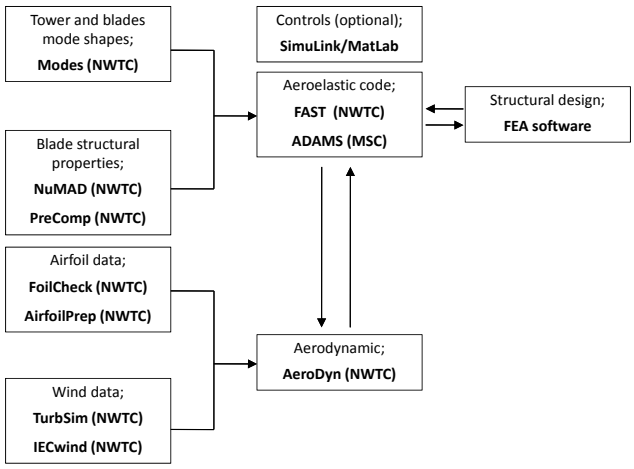

Figure A.1: Design codes overview

bine aerodynamics and structural response are marched through time. This option incorporates operational controls such as blade pitch control, variable-speed torque control, High Speed Shaft (HSS) and tip brakes, and nacelle yaw control. Together with forces and moments acting on the blade roots, FAST determines; i) blade deflections, accelerations, and speed ratios, ii) rotor position (azimuth angle), angular speed and acceleration, iii) Low Speed Shaft (LSS) position, angular speed, acceleration, forces, torque and bending moment, iv) high speed shaft (HSS) angular speed and acceleration, v) nacelle inertia, position, angular speed and acceleration, vi) pitch angle and deflection, vii) rotor and tail furl, viii) tower deflection, velocity, acceleration, moments and forces, ix) platform position, displacement, acceleration, forces and moments, x) rotor power, torque and thrust , and xi) electrical generator torque and power.

The second mode of FAST is a linearization analysis used to determine the modes of operating or stationary HAWTs through eigenanalysis. For more details see FAST User's Guide [38]. For a description of FAST's analytical modelling see [49].

FAST models a three bladed wind turbine using six rigid bodies (earth, nacelle, base plate, armature, hub, and gears), and four flexible bodies (tower, three blades, and drive shaft). The blades and tower are treated as cantilevered beans fixed at one end and free at the other end. Then, the deflection of the tower and the blades are obtained as a linear combination of the shapes of the first normal vibration modes

(modal superimpose analysis). FAST models longitudinal and lateral deflection of the tower caused by bending using two mode shapes, and each tower mode requires 2 DOFs to scale the shape functions. Thus, the tower accounts for 4 DOFs. Blade deformation is modelled with 2 vibration modes in the out-of-plane direction and just 1 mode in the in-plane direction, since the flexibility in this direction is lower. Each blade mode uses 1 DOF, therefore a single blade requires 3 DOFs. FAST regards the mode shapes as sixth-order polynomials with first and second terms equal to zero, since the tower and blade are cantilevered and must have zero displacement and slope in the supported end. Mode shapes are not generated by FAST and must be entered in the respective input file by setting the 4 coefficients of the polynomial for each tower and blade mode. Finally, FAST is linked with the AeroDyn aerodynamic subroutine package distributed by NWTC for calculating aerodynamic forces [50].

Summarizing, a three-bladed wind turbine in FAST requires 24 DOFs; 9 DOFs for the blades, 4 for the tower, 6 DOFs from the translational and rotational motions of the platform relative to the earth inertia frame, 1 DOF for the yawing motion, 1 DOF for the generator azimuth angle, 1 DOF account for the torsional flexibility (spring and damper) between the generator and the hub/rotor, 1 DOF for rotor-furl and 1 DOF for tail-furl. Notice that FAST does not have blade torsional DOFs. More about the definition of degrees of freedom and coordinate systems in FAST is in Wilson 1999 [51].

According to Jonkman [52], ADAMS is more sophisticated than FAST and has many additional features, e.g., ADAMS allows an almost unlimited number of configurations of DOFs, has torsional and extensional DOFs in the blades, and has material (asymmetric composite ply lay-up) couplings in the blades and tower. On the other hand, since ADAMS has more DOFs relative to the modal analysis of FAST, it requires more computational resources.

Finally, the folder CertTest provided by FAST contains the file Baseline_Blade.dat with the blade mode shapes parameters (and a similar file is provided for damped vibration). It also has the distributed (spanwise) blade properties such as; twist, stiffness, mass, and inertias. The file Baseline_Tower.dat contains the same information for the tower. Active pitch control is based on a routine provided for FAST package called PitchCntrl_ACH.f90 located at folder Source inside FAST installation files

A.2 AeroDyn

FAST and ADAMS interact with the AeroDyn code to obtain aerodynamic forces. The aerodynamic estimations are therefore the same for both codes and the difference lies on the structural dynamics. AeroDyn is distributed by the NTWC and uses the quasi-steady blade-element momentum (BEM) theory (incorporating Prandtl's tip and hub losses) or a generalized dynamic-wake (GDW) model. The entire description of the AeroDyn methodology can be found in Moriarty [53] and AeroDyn User's Guide [50]. Here it will be briefly described.

AeroDyn divides the blade into sections along the span and determines the forces acting on each section according to turbine geometry, operational conditions, wind inflow conditions, velocity and location of the blade section, and from the aeroelastic simulation. Then, based on the two dimensional flow acting on the section, and according to the lift, drag and pitching moment coefficients for that airfoil section, AeroDyn determines the aerodynamic forces at each time step. To do so, the code has two options to model the effect of the wake; the blade element momentum theory (BEM) or the dynamic wake theory (DWT). Note that the accuracy of lift, drag and pitching moments are critical for the results and rely on the user to input proper data, particularily near stall and for the entire range of angles of attack (+/- 180°) which are not commonly available. NREL developed the code FoilCheck to generate aerodynamic coefficients for large angles of attack and Reynolds numbers based on flat plate characteristics.

The first option to model the wake, BEM theory, considers each blade section as an independent 2-D flow entity, and then the forces on the entire blade are obtained as the sum of such sections. BEM assumes that the loss of momentum of the flow through the rotor plane is caused by the work done for the passing flow on the blade sections. Therefore, it is possible to estimate the induced velocities in the axial and tangential directions, which determine the inflow and then affecting the forces acting on the airfoil section. This iteration is performed until induced velocities and aerodynamic forces converge at each time step. Paraphrasing Moriarty [53], the main limitations of BEM theory are; i) calculations are static assuming that the flow around the airfoil is always in equilibrium and accelerates instantaneously to adjust the vorticity in the wake, ii) BEM assumes that the blade section is in the rotor plane since momentum in balanced in a plane parallel to the rotor, then deflections introduce error in the

modelling, and iii) BEM neglects spanwise flow since, as was stated before, assumes forces and flow acting in a 2-D section (i.e. BEM theory does not include effects from adjacent blade sections). Additionally, AeroDyn does not include terms for coning angle or teeter of the rotor plane for BEM. Some corrections are introduced to BEM theory for AeroDyn to properly model wind turbine conditions, such as; a) tip-loss theory according to Prandtl's model, b) hub-loss theory which is similar to Prandtl correction, c) a skewed wake correction for wind turbines operating with yaw angles, and d) a Glauert correction to estimate the element thrust for high axial induction factor (a>0.4), as for blade elements near the tip once the tip-loss model is incorporated.

The second option to model the wake in AeroDyn is the generalized dynamic wake theory, which is based on a potential flow solution of Laplace's equation (inviscid and incompressible flow) and consists of an infinite series of Legendre functions in the radial direction and trigonometric functions in the azimuthal direction developed for Kinner (1937) to solve the pressure distribution in the rotor plane. Again quoting Moriarty, the main advantages of GDW over BEM theory include tip losses modeling, skewed wake aerodynamics, and the modeling of the dynamic wake effect which is the lag (time) in the induced velocities created by vorticity radiated from the blade and convecting downstream. Its main limitation, according to Moriarty, is that GDW method only works for lightly loaded rotors where induced velocities are small relative to the free stream. This assumption breaks down at low wind speeds when the turbulent wake is approached. Then, AeroDyn automatically changes to BEM theory at free stream wind speed below 8 m/s to avoid instability. Additionally, since GDW does not consider wake rotation FAST uses BEM equation to calculate the tangential induction factor. Finally, as for BEM theory, GDW assumes the rotor plane as a flat disk and thus, large deflection or coning will produce error in the modelling.

A.3 FAST Simulation

Figure A.2 depicts the operational simulation of a wind turbine of 1.5 MW for different steady wind conditions using FAST. The chart includes below rated wind speeds with variable-speed torque control activated and above rated wind velocities with active pitch control.

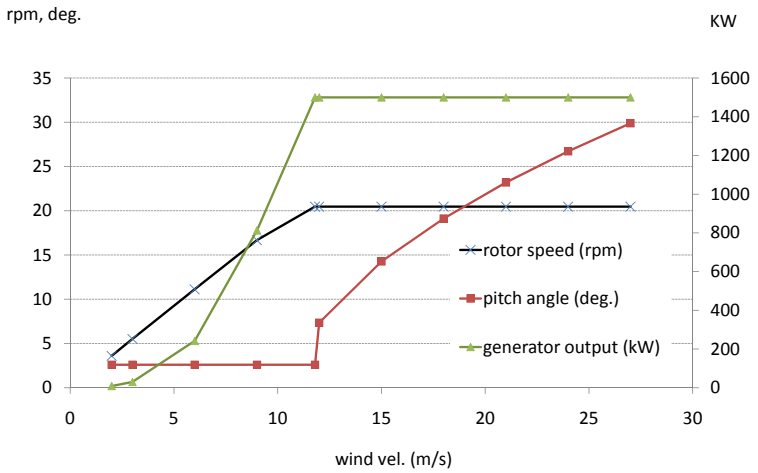

(a) Rotor speed, pitch angle and generator output

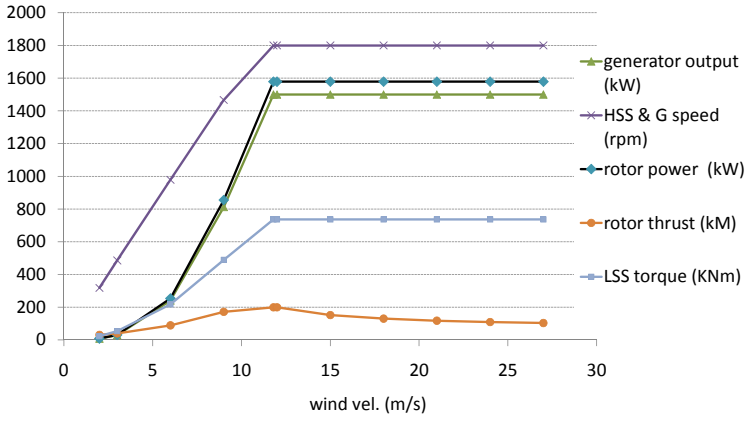

(b) Generator output, High Speed Shaft (HSS), Low Speed Shaft (LSS) torque and rotor power and thrust

Figure A.2: 1.5 MW wind turbine performance for different wind speeds (at hub height)

Additionally, Figure A.3 shows a forty second FAST simulation (between 30 and 70 seconds) at 15m/s and under normal turbulence conditions. Variability in thrust seems to be much more than for rotor torque. Finally, the results show the relevance of body forces for edgewise bending moments and the effect of wind turbulence on flapwise bending moment.

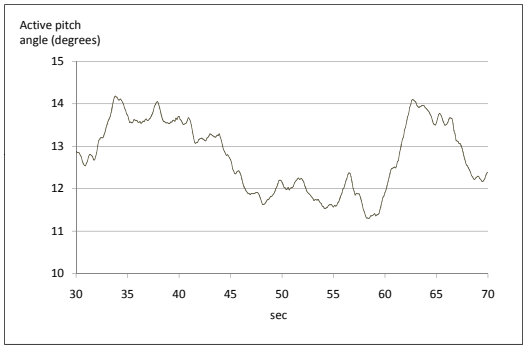

(a)

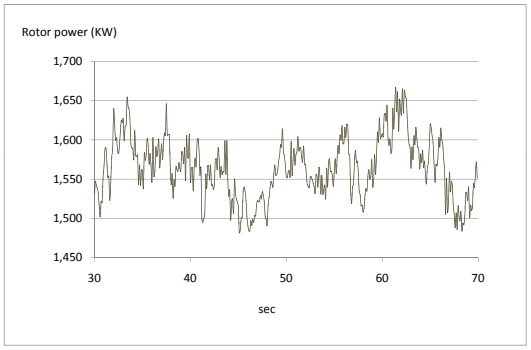

(b)

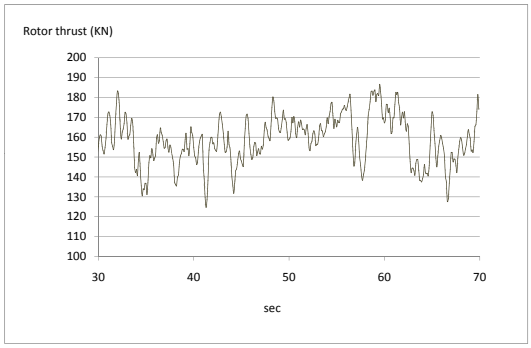

(c)

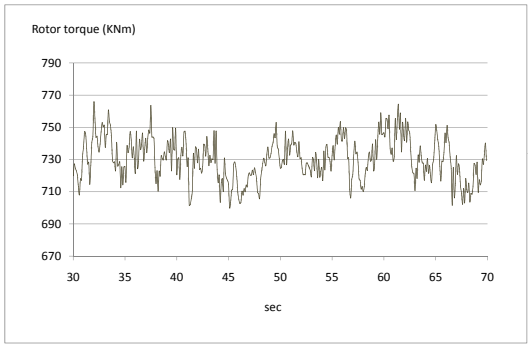

(d)

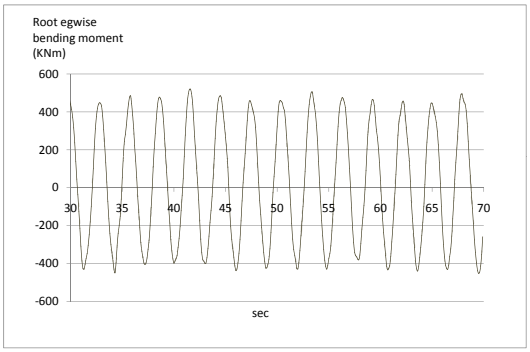

(e)

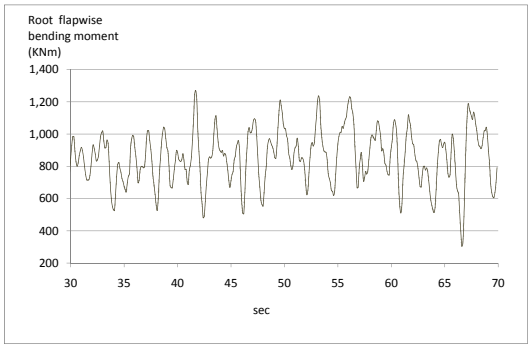

(f)

Figure A.3: WP1.5MW performance at 15m/s under normal conditions

Appendix B

WP1.5MW Blade Definition

The wind turbine blade structure used in this work is based on the WindPACT 1.5 MW Baseline 3-Bladed Turbine (WP1.5MW) described in the WindPACT Turbine Rotor Design Study [37]. The baseline blade model properties of the 1.5 MW turbine is provided by FAST and described here in Table B.1. (For more details see file FAST/CertTest/BaselineBlade.dat)

Table B.1: WP1.5MW Structural Blade Definition

r/R	Twist [deg]	Mass density [kg/m]	Flap Stff $[Nm^2 \times 10^6]$	Edge Stff $[Nm^2 \times 10^6]$	Torsional Stff $[Nm^2 \times 10^6]$
0	11.100	1447.607	7681.46	7681.46	2655.23
0.052	11.100	181.672	1020.62	1092.28	343.81
0.157	11.100	186.138	523.14	833.66	127.19
0.263	9.500	178.321	234.57	614.65	16.80
0.368	6.300	158.222	154.90	435.26	12.64
0.473	3.100	138.123	75.23	255.87	8.48
0.578	2.100	107.669	49.75	179.86	5.76
0.684	1.100	77.215	24.27	103.85	3.04
0.789	0.480	51.861	9.27	54.25	1.38
0.894	0.240	31.607	4.75	31.06	0.78
1.000	0.000	11.353	0.23	7.87	0.18

Appendix C

Blade Structural Design

The wind turbine blade designed in this work is based on the WindPACT 1.5 MW Baseline 3-Bladed Turbine (WP1.5MW) described in the WindPACT Turbine Rotor Design Study [37] and the WindPACT Turbine Design Scaling Studies [41].

Table C.1 describes the structural definition of the blade designed in this work to be implemented in FE modeling.

Table C.2 shows the shell layers in the designed blade which are stated in the WindPACT Turbine Design Scaling Studies [41].

Table C.1: Structural Blade Definition

Airfoil (scaled)	Circular	s818		s825	s826	
Station r/R	7%	25%	50%	75%	95%	100%
Distance from root [m]	0.70	7.00	15.75	24.50	31.50	33.25
Chord [c/R]	n/a	8.0%	6.0%	4.5%	3.0%	2.5%
Chord [m]	1.7	2.800	2.100	1.575	1.050	0.875
Twist (deg)	n/a	10.0	2.5	0.0	-0.03	-0.5
Aerodynamic Offset	n/a	0.30	0.30	0.30	0.30	0.30
Airfoil Thickness [t/c %]	n/a	27%	24%	21%	16%	16%
Airfoil Thickness [m]	n/a	0.76	0.50	0.33	0.17	0.14

Table C.2: Blade Shell Layers [mm]. See Griffin [41]

Layer	Material	Thickness [mm]
1 (Exterior)	gel coat	0.51
2	random mat	0.38
3	triaxial fabric	0.89
4		
0-15% c	balsa	0.5% c
15-50% c	spar cap mixture	5% t/c
50-85% c	balsa	1.0% c
5 (Interior)	triaxial fabric	0.89